Why MagNet: Quantifying the Complexity of Modeling Power Magnetic Material Characteristics

Why MagNet: Quantifying the Complexity of Modeling Power Magnetic Material Characteristics

Diego Serrano, *Member, IEEE*, Haoran Li, *Student Member, IEEE*, Shukai Wang, *Student Member, IEEE*, Thomas Guillod, *Member, IEEE*, Min Luo, *Senior Member, IEEE*, Vineet Bansal, Niraj Jha, *Fellow, IEEE*, Yuxin Chen, *Senior Member, IEEE*, Charles R. Sullivan, *Fellow, IEEE* and Minjie Chen, *Senior Member, IEEE*

***Abstract*—This paper motivates the development of sophisticated data-driven models for power magnetic material characteristics. Core losses and hysteresis loops are critical information in the design process of power magnetics, yet the physics behind them is not fully understood. Both losses and hysteresis loops change for each magnetic material, are highly nonlinear, and depend heavily on the electrical operating conditions (e.g., waveform, frequency, amplitude, dc bias), the mechanical properties (e.g. pressure, vibration), as well as temperature and geometry of the magnetic components. Understanding the complexity of these factors is important for the development of accurate models and their applicability and limitations. Existing studies on power magnetics are usually developed based on a small amount of data and do not reveal the full magnetic behavior across a wide range of operating conditions. In this paper, based on a recently developed large-scale open-source database – *MagNet* – the core losses and hysteresis loops of Mn-Zn ferrites are analyzed over a wide range of amplitudes, frequencies, waveform shapes, dc bias levels, and temperatures, to quantify the complexity of modeling magnetic core losses, amplitude permeability, and hysteresis loops and provide guidelines for modeling power magnetics with data-driven methods.**

***Index Terms*—power magnetics, core loss, B–H loop, hysteresis, data-driven methods, data visualization, open source database**

I. Introduction

MAGNETIC components perform important functions in power electronics in many different ways. Inductors and coupled inductors are required for regulation, to ensure resonant operation, and to achieve soft switching or soft charging. Transformers are needed to provide galvanic isolation and fixed gains. Different magnetic components are required for each application and operating condition. The future development of in-package and on-chip magnetics, as well as magnetics for automotive, industrial, medical, and robotics applications, makes a precise understanding of magnetic materials across wide operation ranges critical [1]–[4].

The design of magnetics components is challenging and often an iterative process mainly because of the large selection of winding structures (winding technology, number of turns, arrangement) and core options (material, shape, size) to choose from. Accurate models for windings exist [5]–[7], but accurate models for the behavior of magnetic materials are limited. Parameters such as permeability, saturation level, or core losses are heavily influenced by electrical, mechanical, and thermal conditions [8], [9].

The most important characteristic of magnetic materials is the relation between the flux density, $B(t)$, and the magnetic field strength, $H(t)$. The relation between $B(t)$ and $H(t)$ is

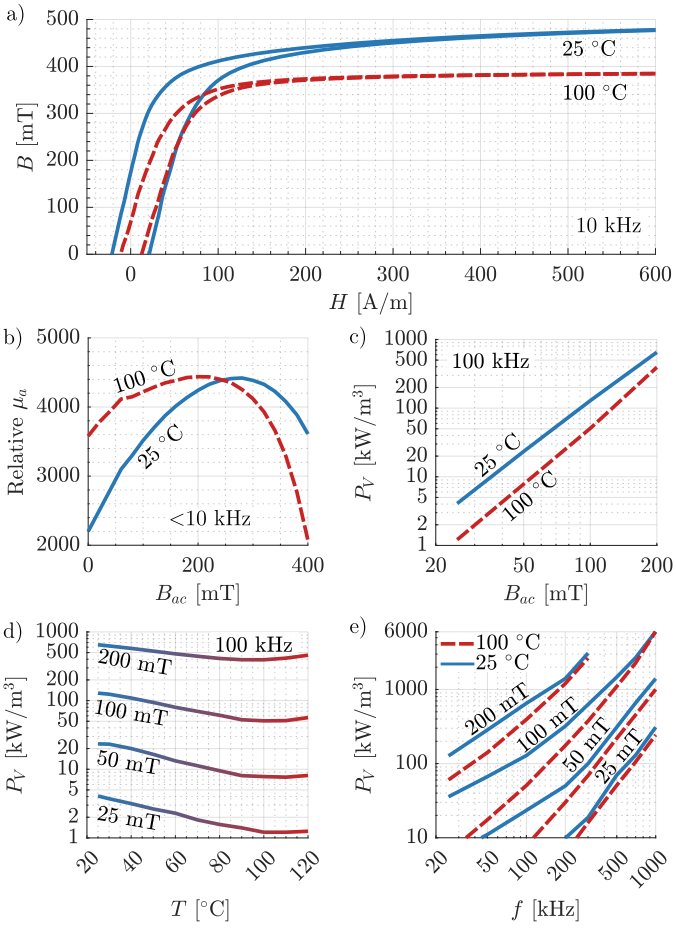

Fig. 1. Relevant information for the material N87 [10] from the manufacturer's software [11]. a) B–H loop for a large excitation at 10 kHz at 25 °C and 100 °C. b) Amplitude permeability for low-frequency excitations. c) Volumetric core loss (P_V) as a function of peak flux density. d) P_V as a function of temperature. e) P_V as a function of frequency.

D. Serrano, H. Li, S. Wang, N. Jha, V. Bansal, and M. Chen are with the Department of Electrical and Computer Engineering and the Andlinger Center for Energy and the Environment at Princeton University, Princeton, NJ, 08540, USA (e-mail: {ds9056, haoranli, sw0123, jha, vineetb, minjie}@princeton.edu).

T. Guillod and C. R. Sullivan are with Dartmouth College, Hanover NH, USA (e-mail: {thomas.paul.henri.guillod, charles.r.sullivan}@dartmouth.edu).

Y. Chen is with the Department of Statistics and Data Science at the Wharton School at University of Pennsylvania, Philadelphia PA, USA (email: yuxinc@wharton.upenn.edu).

M. Luo is with Plexim GmbH, Zurich, Switzerland (e-mail: luo@plexim.com).

usually described as a B–H hysteresis loop. An example of the static hysteresis curve is shown in Fig. 1a. Commonly used design parameters such as amplitude permeability, saturation level, or core losses can be obtained from the B–H loop. Since the B–H loop changes drastically with the excitation waveform and temperature, core loss and amplitude permeability are also affected. Typically, hysteresis loops are included in datasheets for only extreme peak flux density, low frequency, and a few temperatures.

The amplitude permeability, defined as the ratio between the peak-to-peak values of B and H, can be used to estimate the large-signal inductance of ungapped magnetic components. Although the inductance is mainly given by the gap in general, the permeability of the core might be needed for high-frequency inductors where permeability is low and gap is not required, to estimate the inductance of chokes, or to calculate the magnetizing current in transformers, which might impact ZVS in some cases. In datasheets, the amplitude permeability is usually given for a few sinusoidal excitations only (Fig. 1b). Generally, the other plots are dedicated to the permeability for very small B swings. In this paper, the operating conditions affecting the amplitude permeability are investigated to assess whether the datasheet information is sufficient.

Core loss can be obtained from the volumetric energy loss per cycle (the area inside the B–H loop). Core losses can limit the maximum frequency and flux density that magnetic components can handle. The estimation of core losses is also complex, and cannot be obtained from datasheet parameters as usually only a few curves for core loss for sinusoidal waveforms are provided. Figs. 1c-e show typical curves used to estimate core loss from the datasheet. In a few cases, manufacturers provide more data points by other means, such as specific software tools [11], but they are still limited to sinusoidal excitations without dc bias. To make matters worse, core losses are also impacted by the size and geometry of the core, as the magnetic field inside the core can be unevenly distributed, especially at high frequencies [12]–[14].

Traditional datasheets cannot describe the behavior of magnetic materials under a mix of numerous realistic operating conditions. Multi-dimensional interpolations and extrapolations are usually needed, which may introduce large errors. A lot of progress has been made in the development of models for magnetic materials, yet, to date, analytical models cannot effectively cope with all these multi-physics, multi-dimensional effects. Physical models, although broadly able to explain the origins of core losses [12], [15], cannot yield accurate estimates for all circumstances yet and analytical models (physics-based or empirical) are intended for only specific sets of operating conditions. Traditional studies on power magnetics usually start by separating many different impact mechanisms (e.g., waveform, temperature, dc bias) and focus on one or a few mechanisms only. In this paper, we demonstrate that modeling each individual factor independently may not result in a unified model with sufficient accuracy and generality, and cannot lead to an accurate magnetic design tool. A sophisticated modeling framework that is powerful enough to capture many factors and their correlated impact is necessary to fully replicate the behaviors of magnetic materials and provide useful guidelines. The main contributions of this paper are: (1) Quantifying and visualizing a large database of measurements to determine how different factors affect magnetic material behavior using the Mn-Zn ferrite material N87 as an example. (2) Reviewing the literature for each one of the parameters affecting the behavior B–H loops and core losses. (3) Using the data to demonstrate the coupling between the different parameters affecting core losses and motivate the development of large-scale sophisticated data-driven models.

This paper helps to demonstrate the complexity of power magnetics modeling and provides a motivation for developing more sophisticated models, such as neural networks, as the primary focus of [16]. The rest of the paper is structured as follows: Section II presents the methodology used to acquire and process the data. In Section III, the vast amount of data is evaluated and visualized, discussing each of the key factors affecting the magnetic behaviors, including flux density, frequency, waveform shape, dc bias, temperature, core geometry, and core material. The effects of combining several parameters together are discussed in Section IV. Finally, Section V concludes this paper.

II. Data Preparation

One major obstacle for data-driven models of magnetic materials is that only a small amount of high-quality data is available in the vendor's datasheets. A large-scale open-source power magnetics database – *MagNet*[1] – has been constructed recently to provide a common ground for data-driven characterization for power magnetics [18]. Details about this database and its construction are provided in a separate paper [16]. For completeness, the setup used to obtain the measurements and the methods to process the data are included below, as a summary of [16]:

A. Hardware setup

The two-winding method (also referred to as the V–I method or the voltamperometric method) is the most common procedure for B–H loop and core loss characterization [19]–[26]. Two separated windings are used; a voltage excitation is applied to the primary and its current is measured to obtain H. The voltage across the secondary winding is measured to obtain B. This method is capable of capturing B–H loops under arbitrary excitation waveforms, but is sensitive to time delays between the voltage and current measurement. This delay and other sources of errors affecting this solution are detailed in the Appendix. This method is selected as data collection can be easily automated since the setup does not need to be modified for each operating condition tested.

Fig. 2 shows a block diagram of the experimental setup. The different parts are described below and are designed following the recommendations in [19], [20], [27].

- **Device under test (DUT):** For most of this paper, a toroidal core of 34 mm outer diameter, 20.5 mm inner diameter and 12.5 mm height (designated R34.0×20.5×12.5 by the manufacturer) of the material

[1]Mag-Net Website: mag-net.princeton.edu [17]

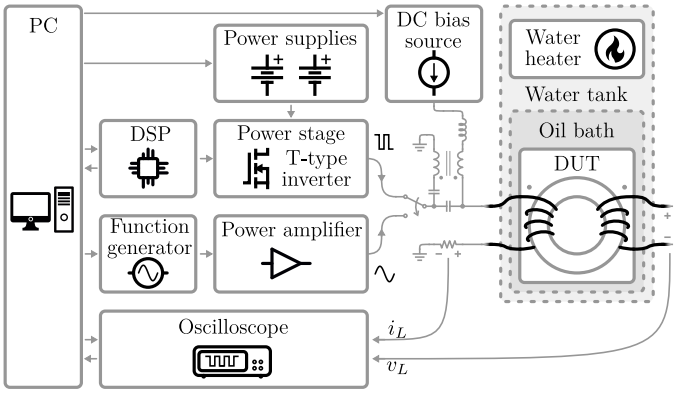

Fig. 2. Block diagram of the automated setup highlighting how the different equipment is interconnected.

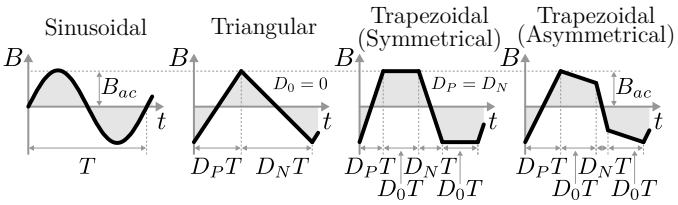

Fig. 3. Waveform shapes together with the definition of the duty cycles used throughout the paper.

N87 from TDK is studied [10]. In MagNet, 142,871 voltage and current pairs of waveforms for different operating conditions are included for this core.

- **Excitation:** The DUT is excited with sinusoidal, two-level pulse-wide-modulated (PWM), and three-level PWM voltages, leading to sinusoidal, triangular, and trapezoidal (symmetric and asymmetric) B waveforms (see Fig. 3). Sinusoidal waveforms are obtained using a power amplifier (Amplifier Research 25A250AM6) taking the reference from a function generator (RIGOL DG4102). A T-type inverter with GaN switches (GaN Systems GS66508B) supplied by two voltage sources (B&K Precision XLN60026) is used for triangular and trapezoidal excitation. The duty cycles, defined in Fig. 3, are iterated in 10% steps. A 100 µF 100 V film capacitor is placed between the power stage and the DUT to block the average voltage of the switching node to create asymmetrical PWM waveforms. For each waveform shape and temperature, the flux density and frequency are swept in the ranges and steps represented in Fig. 4.
- **Dc bias:** To bias the core, a direct current is injected into the primary winding, after the series capacitor. A transformer and a filter inductor are added to prevent the reflected voltage of the DUT from being applied to the current source (Fig. 2). The current source is a voltage supply (Siglent SPD3303X-E) controlled in current mode. Fig. 4 also shows how the dc bias is iterated in the testing procedure. Note that a direct current is applied, defining H_{dc} rather than B_{dc}. B_{dc} is not reported in this work as there is no explicit relation between H_{dc} and B_{dc} [19] and it cannot be calculated using the current measurement scheme.

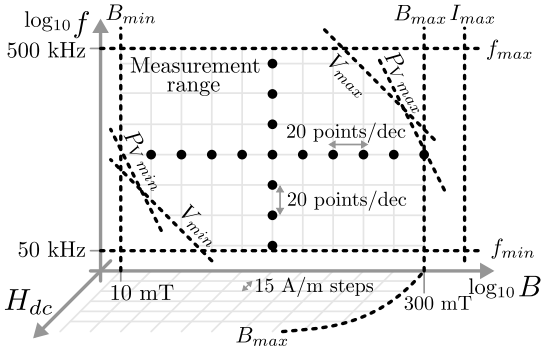

Fig. 4. Range for the tests for the B_{ac}, f and H_{dc} variables.

- **Data acquisition:** The measurements for the voltage and current waveform are acquired with an 8-bit oscilloscope (Tektronix DPO4054). 100,000 samples are saved for each test, with a total sample time of 80 µs. The bandwidth of the measurement is limited to 20 MHz to avoid excessive switching noise in the triangular/trapezoidal waveforms due to the fast switching transitions. A low capacitance passive probe (Tektronix P6139A) and a coaxial shunt (T&M Research W-5-10-1STUD) are employed for voltage and current measurement, respectively.
- **Temperature control:** Keeping a controlled temperature is critical since core losses are temperature-dependent and core losses during testing heat up the core. The DUT is submerged in a mineral oil bath with a magnetic stirrer (INTLLAB) to keep the core close to the oil temperature. The oil bath is inside a water tank and its temperature is controlled using a water heater (Anova AN400-US00). Measurements are collected at 25 °C, 50 °C, 70 °C, and 90 °C water temperature. In this work, the water temperature is used to report the core temperature, although small variations between the two temperatures are present during testing as mentioned in Appendix E.

The automation and synchronization of different instruments are managed by a Python script. Additionally, there are limitations associated with the power stage/power amplifier. The voltage range for the tests is 1 V to 50 V for sinusoidal waveforms and 5 V to 80 V for PWM waveforms (Fig. 4), which limits the $B_{ac} \cdot f$ product of the data points measured, especially for extreme duty cycles. More details of the hardware setup are included in [16]. Moreover, a complete error analysis for this setup is provided in the Appendix.

B. Data processing

The stored voltage and current measurements are processed to obtain the B and H waveforms and other parameters of interest (f, B_{ac}, D_P, D_N, H_{dc}, and P_V) in the following order:

- **Data downsampling:** To compress the data, the measurements are downsampled from 100,000 to 10,000 samples per test using a boxcar averaging algorithm, which simply takes the average of each consecutive 10 samples. This reduction in data size increases the effective

vertical resolution of the measurement at the expense of horizontal resolution [22].

- **Fundamental frequency:** There might be a slight difference between the commanded frequency for the equipment and the actual frequency of the signal applied. With a sampling time of 8 ns and 10,000 samples, the resolution of fast Fourier transform (FFT) is only 12.5 kHz, rendering the FFT imprecise to calculate the fundamental frequency. Instead, the power spectral density of the signal is estimated using Welch's method [28]. The highest peak in the power spectral density near the commanded frequency corresponds to the fundamental frequency of the excitation signals.
- **Single-cycle voltage and current:** Since the total sampling time is fixed to 80 µs, a different number of switching cycles is captured depending on the frequency of the excitation. The size of the database is further reduced by extracting a single-cycle waveform based on the detected fundamental frequency. To do so, the measured voltage and current waveforms are split into the different switching cycles sampled. These cycles are interpolated into 1,024 samples per cycle and then the average waveform of the different switching cycles is obtained. To avoid artifacts, data is discarded based on the similitude of different cycles. More technically, when either the voltage or current waveform error as defined by Eq. 1 is above 10%, the complete data point (and all its samples) is discarded.

$$\text{error} = \frac{\sum_{i=1}^{N_{\text{cycles}}} \sum_{n=1}^{1024} \left(A_{i,n\ \text{meas}} - A_{n\ \text{averaged}}\right)^2}{N_{\text{cycles}} \sum_{n=1}^{1024} A_{n\ \text{averaged}}^2} \tag{1}$$

Where $A_{i\ \text{meas}}$ is the measured voltage or current waveform of the i^{th} cycle, A_{averaged} is the resulting voltage or current waveform after averaging, and n is the sample. Fig. 5a-b shows one example of the resulting single-cycle voltage and current waveforms. Any dc offset in the voltage waveform is removed.

- ***B* and *H* waveforms:** The rest of the parameters are obtained from the single-cycle voltage and current. Flux density is calculated by integrating the voltage using Eq. (2). However, the initial value of B cannot be obtained with this method since the voltage is not captured from the time that the excitation is first applied (as in [23]) but only on steady-state conditions. Because of this issue, in this work, B is defined so that its average value B_{dc} is 0, even for data with $H_{dc} \neq 0$.

$$B^*(t) = \frac{1}{A_e \cdot n_2} \int v_L(t)\,\mathrm{d}t\ ;\ B(t) = B^*(t) - \overline{B^*} \tag{2}$$

Where B^* is the flux density before its average value is removed. The data is reported as a function of the amplitude of $B(t)$, B_{ac}, defined as $(B_{max} - B_{min})/2$. The H waveform is obtained from current measurements using Eq. (3). H_{dc} is defined as the average of $H(t)$ rather than as $(H_{max} + H_{min})/2$.

$$H(t) = \frac{n_1}{l_e} i_L(t)\ ;\ H_{dc} = \overline{H} \tag{3}$$

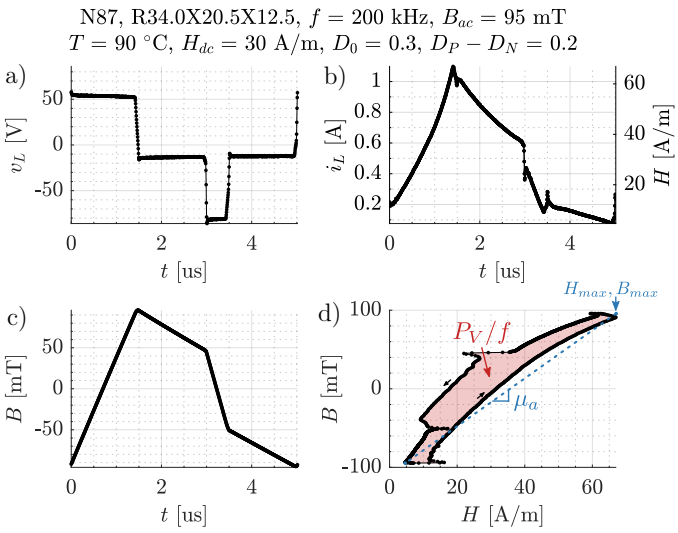

Fig. 5. Processed measurements for a random asymmetric trapezoidal waveform. a) Measured voltage. b) Measured current and field intensity. c) Flux density. B_{dc} is not included. d) B–H loop highlighting P_V and μ_a as defined in Eq. (5).

The effective parameters l_e, A_e, and V_e are obtained from the manufacturer's datasheet but can also be calculated following the IEC Standard 60205 [29]; see Eq. (8). An example of the B and H waveforms pairs is shown in Fig. 5b-c, respectively.

- **Core loss:** Core losses are obtained directly from the average of the product of the voltage and current waveforms [25]. For the volumetric core loss, the obtained value is divided by the effective volume of the core V_e. Alternatively, volumetric core losses per cycle can be calculated from the integral of $H(t)$ over $B(t)$ [30] (see Fig. 5d).

$$P_V = \frac{f}{V_e} \int_0^{\frac{1}{f}} v_L(t) \cdot i_L(t)\ \mathrm{d}t = f \oint H(B)\ \mathrm{d}B \tag{4}$$

- **Amplitude permeability:** The amplitude permeability can be used to obtain the relation between the volt-second and the current ripple together with the number of turns. It is directly calculated from the peak to peak B and H:

$$\mu_a = \frac{B_{max} - B_{min}}{H_{max} - H_{min}} \tag{5}$$

Note that the peak in B and H can be reached at slightly different times. As a result, the H_{max}, B_{max} point in the B–H plot might not be a point of the B–H loop itself (see Fig. 5d).

Further details on the post-processing of the data, such as the calculation of the duty cycles, are available in [17]. Throughout the rest of the paper, B–H loops, volumetric core loss, and amplitude permeability are visualized and studied under different operating conditions and external factors. Sometimes the data does not form a perfect grid due to a small deviation of the commanded B_{ac}, f, H_{dc}, and duty cycles from the measured ones. To properly depict volumetric core loss and amplitude permeability as a function of other variables, interpolation is required. A linear interpolation is applied to

$\log(B_{ac})$ and $\log(f)$, duty cycle, H_{dc}, and temperature for $\log(P_V)$ and $\log(\mu_a)$, after a Delaunay triangulation of the points. Interpolation is reliable as long as enough data points are collected to capture the trends. One should be wary of extrapolation because patterns might change. As such, the data is not extrapolated.

III. The Complexity of Power Magnetics Modeling

In this section, the individual effect of frequency, amplitude, waveform shape, dc bias, temperature, core size, and material in B–H loops, core losses, and permeability are investigated one by one using the extensive data in MagNet. Later, in Section IV, joint effects are discussed.

A. Frequency and peak flux density in sinusoidal waveforms

At low frequencies, the quasi-static hysteresis is the dominant effect determining the B–H relationship. Physics-based microscopic models, such as the one presented in [12], are sometimes less practical than empirical models. The most commonly used models for B–H loops include the Preisach model, derived from the theory in [31], and the Jiles-Atherton model [32]. A detailed description of common models is included in [33]. Dynamic models are also studied, for instance, an empirical method parameterized with measurements is described in [34]. Methods based on neural networks intended for low-frequency fields or sinusoidal excitations are also proposed in [35], [36].

Fig. 6 provides an example of measured B–H loops for sinusoidal waveforms at increasing flux density and frequency. In general, peak flux density has a significant impact on the area of the loop and affects amplitude permeability. Frequency makes B–H loops have a more ellipsoidal shape with respect to the static hysteresis curves, while barely changing the amplitude permeability.

To visualize the complex behavior of core losses for sinusoidal waveforms of different frequencies and peak flux densities, Fig. 7a presents the data extracted from the MagNet database. Figs. 7b-c shows the same data in the form that is commonly presented in datasheets.

The volumetric core loss for sinusoidal excitations is typically estimated using the Steinmetz equation [37], $P_V = k \cdot f^{\alpha} \cdot B_{ac}^{\beta}$, where the Steinmetz parameters, k, α, and β are constants that can be obtained by curve-fitting data for each material. However, this simple yet effective equation has known limitations: it is only applicable to sinusoidal excitations; it is not accurate across wide frequencies [37], [38]; its accuracy is largely influenced by the data and methods used to extract the Steinmetz parameters. To better understand its accuracy, the measured core losses can be compared to the prediction using the Steinmetz equation when k, α, and β are selected to best fit the measured data (i.e. minimize the total mean square error between the core loss of the complete set of sinusoidal measurements and the predicted loss [39]). Fig. 8 shows the ratio between the predicted and measured losses. This plot highlights how core losses deviate from a simple power law fitting for pure sinusoidal excitations, with errors above 20% in certain B–f regions. Please note that

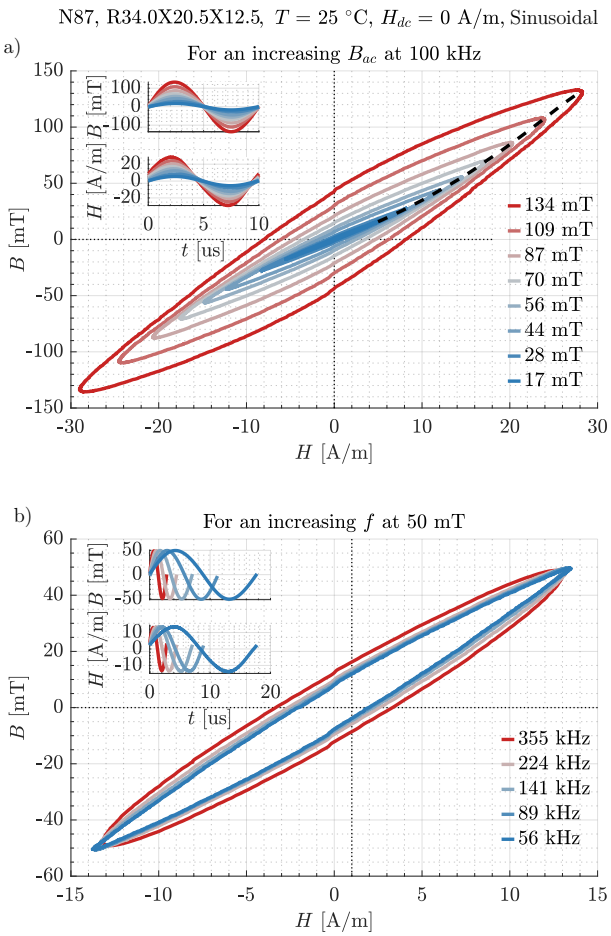

Fig. 6. Measured B–H loops for sinusoidal excitation at 25 °C without dc bias. a) For different flux density amplitudes at 100 kHz. The peak B and H for all waveforms are joined with the discontinuous line to show the change in amplitude permeability. b) For different frequencies at 50 mT. The voltage waveforms are not perfect sinewaves, especially at high flux density due to the use of a power amplifier. Only measurements with low THD (<5%) in the voltage waveform are included to avoid the effects of distortion. Moreover, only data at relatively low $f \cdot B_{ac}$ is available due to the limited excitation voltage.

part of this variation can be the result of small changes in the temperature of the core during testing; this error is explained in Appendix E. More advanced models for core losses can be devised; a common approach is to separate the loss into different components (e.g. hysteresis loss, eddy current loss, relaxation loss, residual loss) based on the physical phenomena responsible for each one [12], [15], [30], [34], [39]–[42]. The database could be used to fit or evaluate these methods.

The data in MagNet can also be processed to obtain the amplitude permeability under different operating conditions. Fig. 9 shows the amplitude permeability (μ_a) in the f–B_{ac} plane for the N87 material at 25 °C for sinusoidal excitation without dc bias. In a large portion of the measurement range, frequency does not impact the permeability substantially while peak flux density does. These measurements show good agreement with the datasheet information in Fig. 1b in the 60 kHz to 300 kHz range, showing that the datasheet information might be enough to capture μ_a for sinusoidal excitations.

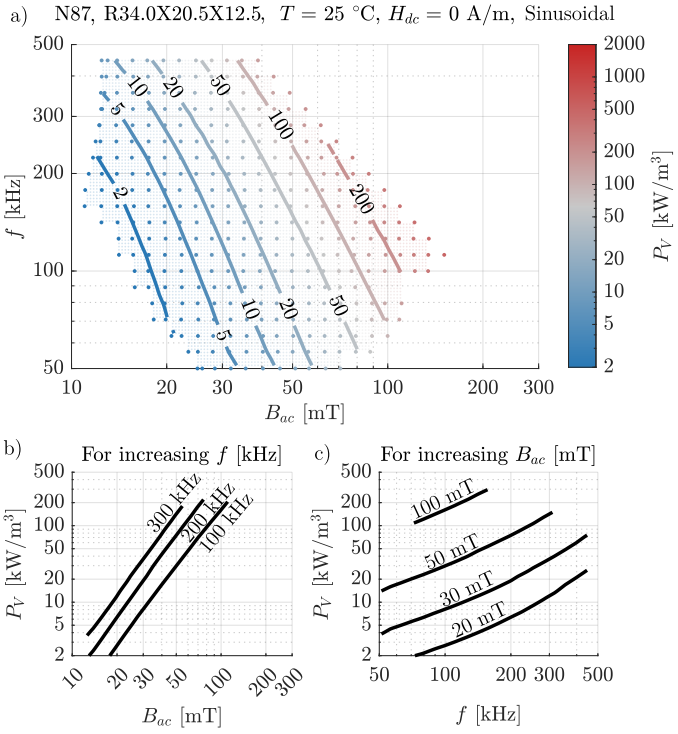

Fig. 7. Volumetric core losses for sinusoidal excitations at 25 °C without dc bias for data with $THD|_V < 5\%$. a) As a function of B_{ac} and f (termed f–B_{ac} plane). Each dot is a measured value. The contours are based on the interpolation of the measurements. b) For various frequencies as a function of B_{ac}. c) For various B_{ac} as a function of f.

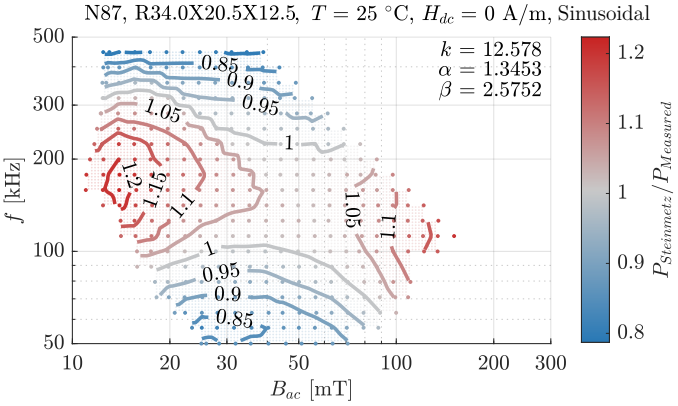

Fig. 8. Variation of the core losses between the prediction using the Steinmetz equation and the measurements. The Steinmetz parameters are obtained using the least-squares method for $\log_{10}(P_V)$ considering all the measured points (dots in the plot). A larger deviation would be obtained if other sets of Steinmetz parameters were used.

B. Effect of waveform shape

Most magnetics in power electronics are excited by sinusoidal or PWM voltage ($\mathrm{d}B/\mathrm{d}t$) [15], [19], [26], [30], leading to distorted sinusoidal, triangular, trapezoidal, or piecewise linear current (H). In this section, we begin the examination of the impact of waveform shape by considering data for triangular $B(t)$ with 50% duty cycle. Fig. 10 shows the measured B–H loops for triangular waveforms with 50% duty cycle, which are noticeably different from the sinusoidal measurements in Fig. 6, especially as sharp changes in $H(t)$

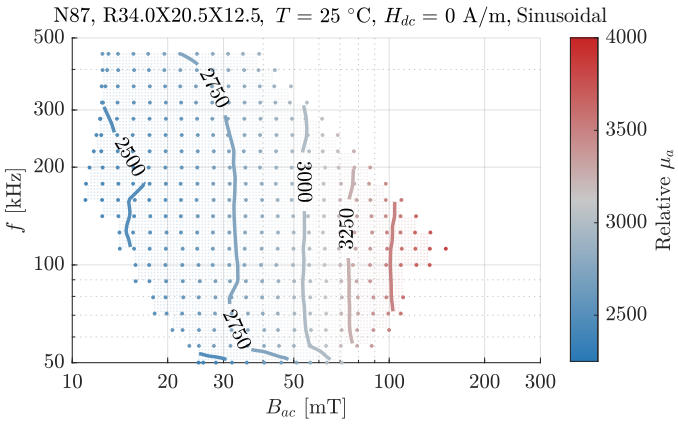

Fig. 9. Relative amplitude permeability (5) as a function of B_{ac} and f for sinusoidal excitations without dc bias at 25 °C. Interpolation is used to graph the contour plots.

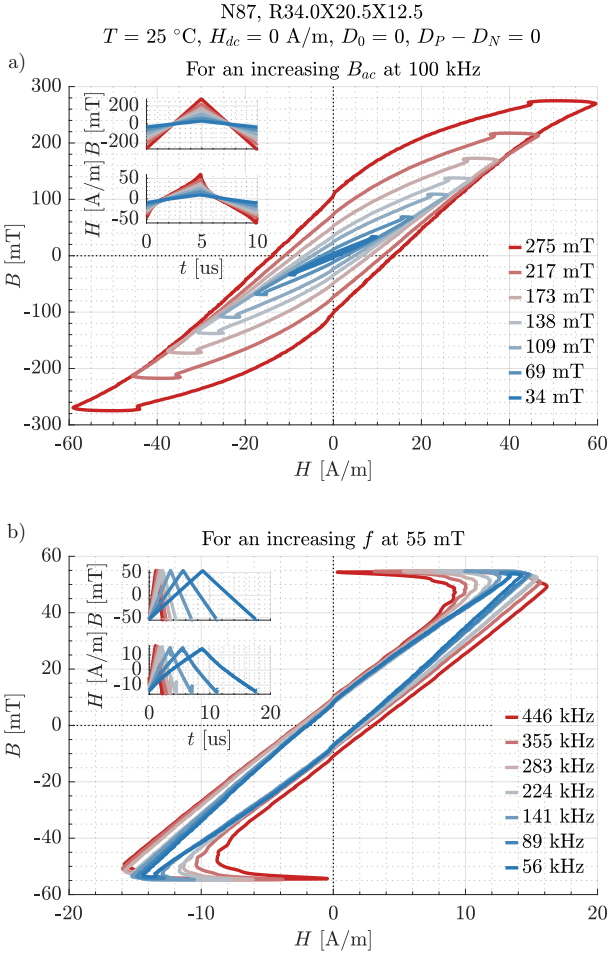

Fig. 10. Measured B–H loops for triangular 50% duty cycle excitations at 25 °C without dc bias. This plot is used as a reference for comparison with other B–H loops throughout the paper. a) For different flux density amplitudes at 100 kHz. b) For different frequencies at 55 mT.

when $B(t)$ reaches its peak. These peaks are affected by the transition speed of the voltage excitation ($\mathrm{d}v/\mathrm{d}t$).

For 50% duty cycle, core losses are shown in Fig. 11. At first glance, the results do not differ much from the sinusoidal measurements (Fig. 7) showing that the power law behavior is

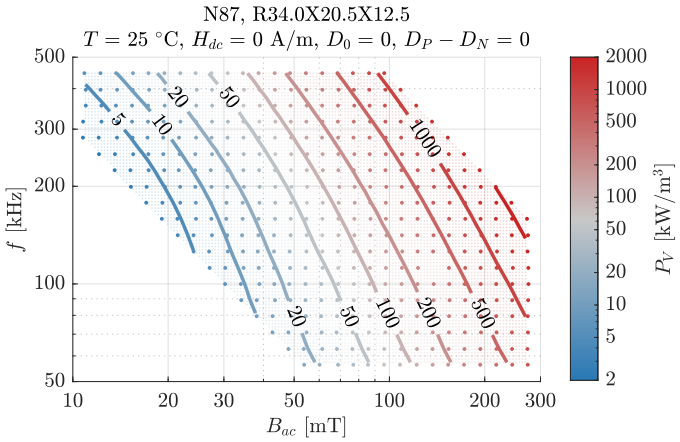

Fig. 11. Core losses for a triangular 50% duty cycle excitation at 25 °C without dc bias as a function of B_{ac} and f. The contour is based on the interpolation of the measurements (each dot).

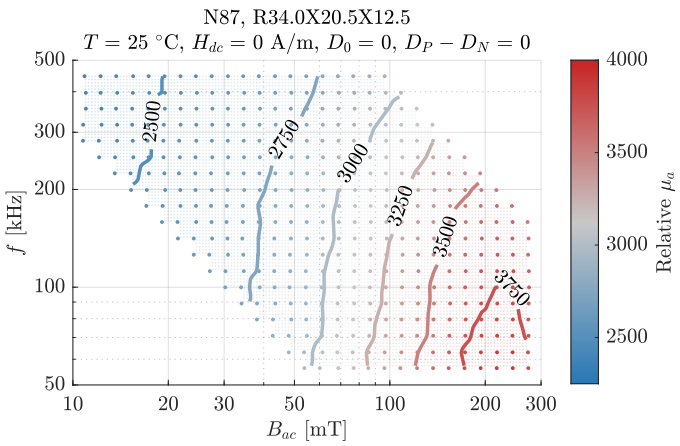

Fig. 12. Relative amplitude permeability as a function of B_{ac} and f for a triangular excitation with 50% duty cycle without dc bias at 25 °C.

still dominant, but again, contour lines are not straight. Note the additional B–H loop area due to fast switching transitions can affect these results.

Finally, Fig. 12 shows the relative amplitude permeability for 50% duty cycle triangular waveforms. The ringing in $H(t)$ during the switching transitions could affect the accuracy of the reported μ_a, but in most cases, the peak does not change B_{max} or H_{max}. Only data where ringing does not affect the reported μ_a is plotted in this paper. Frequency has a larger effect in triangular waveforms as compared to sinusoidal waveforms (Fig. 9), but the main behavior is still governed by the relation between B_{ac} and μ_a given in Fig. 1b.

C. Impact of $\mathrm{d}v/\mathrm{d}t$ during the switching transition

Any measurement with a nominally rectangular voltage waveform has a finite voltage slew rate ($\mathrm{d}v/\mathrm{d}t$) during each transition. Fast transitions may affect magnetic losses, even if the circuit were ideal and did not exhibit ringing. This effect has not been addressed in detail in the literature but was briefly discussed in [19]. The influence of $\mathrm{d}v/\mathrm{d}t$ on the B–H loop is hard to quantify for all possible scenarios. Here, a comparison for a given operation point is provided. Since the waveforms are more severely affected at higher frequencies (Fig. 10b), 500 kHz is selected as the frequency for the test. In this test, the switching speed is changed by loading the switching circuit with different external inductors, which increases the available current during the transition for zero-voltage switching (ZVS). The dead time is set to 100 ns and the input voltage is held constant, although the voltage applied to the DUT changes slightly because of the voltage drop in the power stage. Fig. 13a shows voltage and current, where the effect of the transition is highlighted. The measured current has a peak because of the $\mathrm{d}v/\mathrm{d}t$. These peaks are also reflected in the B–H loops (Fig. 13b), changing the area inside the loop. The capacitance is a combination of the core capacitance due to its material properties and the probe capacitance and winding capacitance (primary and secondary). Measuring this effect properly is not possible with this setup because the winding and core capacitances are expected to be of similar order of magnitude. The total contribution of this effect to losses is also hard to quantify because the voltage waveform is modified by the ZVS transition and the total load current, leading to slightly different B_{ac}. The ratio between the losses of each waveform and the losses at the lowest $\mathrm{d}v/\mathrm{d}t$ among them is shown in Fig. 13c. B_{ac} also changes, but even after accounting for its effect by assuming losses proportional to B_{ac}^{β}, an increase in losses of 6% is obtained just by increasing $\mathrm{d}v/\mathrm{d}t$ from around 1 V/ns to 5 V/ns. The noticeable difference in B–H loop for excitations with different $\mathrm{d}v/\mathrm{d}t$ requires special attention from circuit designers, especially with the extreme switching speed of wide-bandgap devices. The switching speed in this test is fairly low for what GaN devices can achieve, so the impact on real applications might be even more significant. Usually, B–H loop measurements are done with lower $\mathrm{d}v/\mathrm{d}t$. Similar figures where the impact of the transition is negligible with ZVS operation can be found in [19], [43].

D. Impact of duty cycle in triangular waveforms

In this section, the effect of the duty cycle in triangular waveforms is illustrated in detail. Fig. 14a shows B–H loops with duty cycle from 0.2 to 0.8. The results are shown as a function of $D_P - D_N$. D_P is the duty cycle of the positive $\mathrm{d}B/\mathrm{d}t$ period, and D_N is the duty cycle of the negative $\mathrm{d}B/\mathrm{d}t$ period (see the axes in Fig. 14b for clarification). The duty cycle affects $\mathrm{d}B/\mathrm{d}t$, impacting B–H loop area, and hence losses (see Fig. 14b).

Fig. 15 illustrates how B–H loops change as f and B_{ac} change for a large duty cycle (80%). During the relatively long time when the current increases (D_P/f), the B–H loop section remains close to the quasi-static loop. In contrast, the loop area is heavily influenced by the short time where $B(t)$ is decreasing quickly (D_N/f). Fig. 15b shows how the impact of frequency is very significant in this rapidly changing region. Clearly, $\mathrm{d}B/\mathrm{d}t$ largely determines the shape of the B–H loop. At high flux density, the current is distorted and there is a significant difference between magnitudes of the negative and positive peak values of H. Note that the impact of hard-switching transitions seems significant when the duty cycle is extreme and frequencies are high (see the red curve

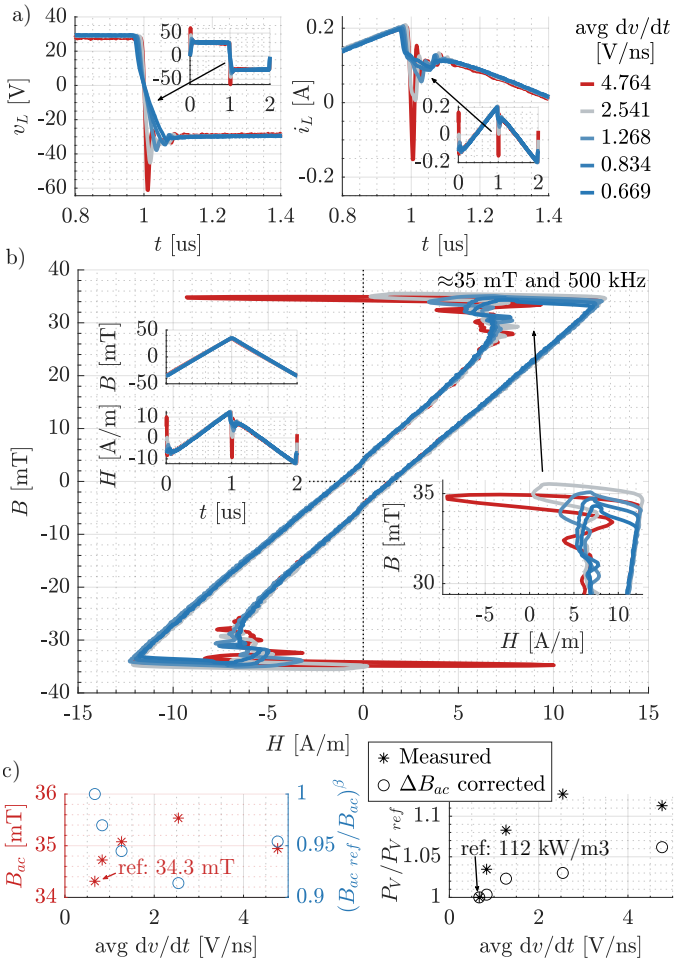

Fig. 13. Effect of $\mathrm{d}v/\mathrm{d}t$ tested with triangular 50% duty cycle excitation at 25 °C without dc bias. a) Zoom of the voltage and current of the DUT with the full waveform as an inset. b) B–H loops, including a zoom where the peak is better observed. c) Calculated B_{ac} and ratio used to compensate the losses. d) Measured losses and losses corrected for B_{ac}, normalized to the test with the lowest $\mathrm{d}v/\mathrm{d}t$. The effect of this small variation in B_{ac} in losses for $\beta = 2.5752$ is included to clarify that there is some impact associated with $\mathrm{d}v/\mathrm{d}t$ in the B–H loop.

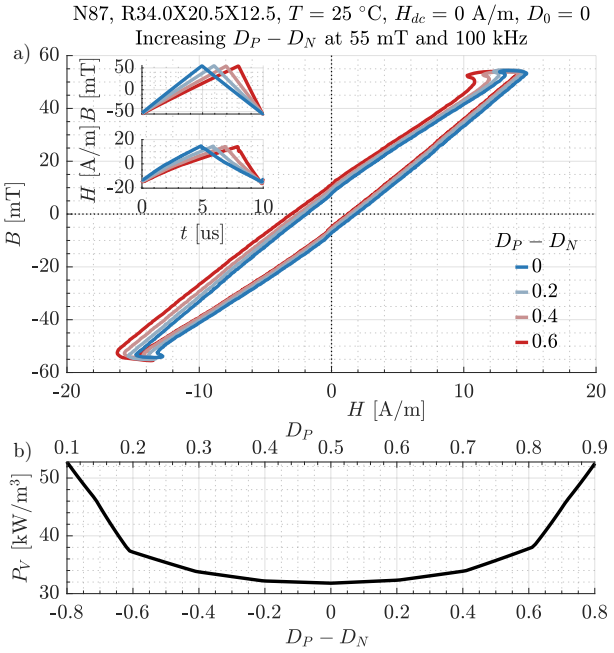

Fig. 14. a) Measured B–H loops for triangular waveforms of different duty cycles at 25 °C, 100 kHz, and 55 mT without dc bias. b) Effect of duty cycle on core losses for the conditions listed above.

in Fig. 15b, with a maximum $\mathrm{d}B/\mathrm{d}t$ of around 5 V/ns), partly because a higher voltage is required for a given B_{ac}, which implies higher $\mathrm{d}v/\mathrm{d}t$; partly because the resonance and decay in H after the transition represent a larger fraction of the falling time.

Duty cycle heavily impacts core losses. Many models have been developed to capture the impact of waveform shapes on core losses. A review of state-of-the-art core loss models for other excitations can be found in [30], [43], [44]. One common approach is to reuse Steinmetz parameters and extend the Steinmetz equation to arbitrary waveforms. This is the basis for models such as the modified Steinmetz equation [40], generalized Steinmetz equation [22], the improved generalized Steinmetz equation (iGSE) [45], and the improved improved generalized Steinmetz equation [30]. Further discussion on this topic is available in [24], [46], [47]. For its simplicity, the iGSE remains the preferred method for core loss calculations. Yet all these methods rely on the Steinmetz parameters, which are only accurate over limited frequency ranges and their choice can determine the accuracy [44], [48]. Methods that rely directly upon measured data are also proposed. In [26], the composite waveform hypothesis, the assumption that the energy lost in each of the sections of a waveform can be added up, is introduced and applied to calculate losses in triangular waveforms of different duty cycles. A curve fit for this approximation is implemented in [44].

The MagNet dataset can be used to evaluate the applicability and limitations of these methods. Fig. 16a shows the volumetric core loss for triangular waveforms with 80% duty cycle. The effect of duty cycle at different f and B_{ac} can be understood by comparing this figure with Fig. 11. The ratio between the losses at 80% duty cycle and 50% duty cycle is shown in Fig. 16b to help compare the data. An important observation is that losses are not just increased by a constant factor depending on the duty cycle but rather are a function of f and B_{ac}, by a factor ranging from nearly 1 to 2 in this specific measurement range. This contradicts the results expected from iGSE if constant Steinmetz parameters are used. For triangular waveforms, P_V is proportional to $D_P^{1-\alpha}+D_N^{1-\alpha}$ for a given B_{ac} and f. These results highlight the need for α to depend on frequency at least.

The database can also be used to evaluate the composite waveform hypothesis [26]. For instance, the results from triangular waveforms at 70 kHz and 400 kHz can be used to estimate the losses for waveforms with a 15.4% duty cycle at 122 kHz. For 30 mT, the energy per cycle at 70 kHz is approximately 73.6 mJ/m^3 and at 400 kHz it is 131.1 mJ/m^3, while for 15.4% duty cycle and 122.3 kHz, the interpolated energy per cycle is 99.4 mJ/m^3. The estimated energy per cycle based on the hypothesis is 102.4 mJ/m^3, an excellent match (3% error) in this specific example. The same procedure can be applied to all data points in Fig. 16; the results, available only

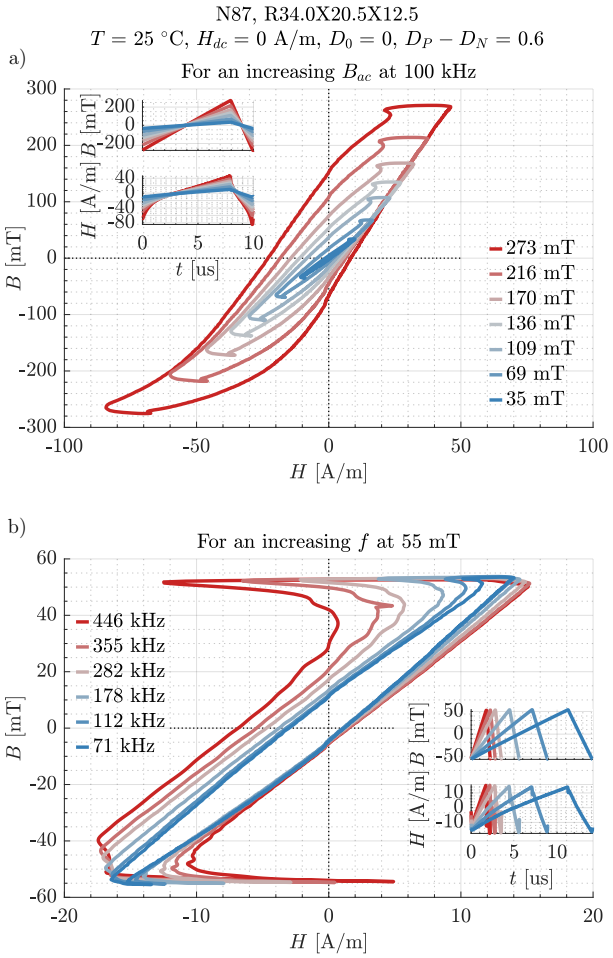

Fig. 15. Measured B–H loops for a triangular 80% duty cycle excitation at 25 °C without dc bias. a) for different flux density amplitudes at 100 kHz. b) for different frequencies at 55 mT. Please compare it with Fig. 10.

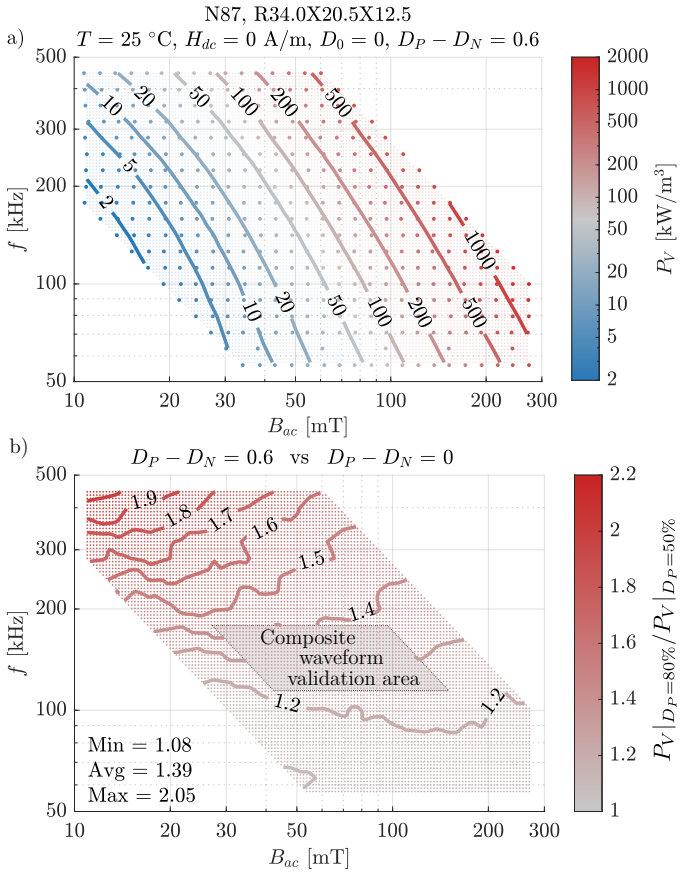

Fig. 16. Effect of duty cycle in volumetric core losses. a) Core losses for triangular 80% duty cycle excitations without dc bias at 25 °C as a function of B_{ac} and f. b) Ratio between P_V at 80% duty cycle and 50% duty cycle. The composite waveform hypothesis has been tested in the marked area.

in the marked area, are underestimated by 2.4% on average, with a maximum discrepancy of 6.4% and a mean absolute error of 2.7%. This example shows that reasonable predictions of losses can be obtained based solely on 50% duty cycle data.

The proposed model in [43] can also be evaluated using this database. In this model, core loss is described as the product of two independent factors, the static hysteresis loss, related to the amplitude and bias of the flux density, and another factor related to the waveform shape and frequency. Using the constants provided in [49] for the volumetric energy loss per cycle without dc bias and at 25 °C, the results for 80% duty cycle can be obtained. Losses are underestimated only by 5.3% on average when compared to the interpolated data, in the range 50 mT to 300 mT and 50 kHz to 400 kHz (from which the parameters are obtained). The maximum absolute error is 30% and the mean absolute error of 7.3% for this specific example. Since two different datasets are compared, different core sizes and core-to-core variation can also contribute to the reported error, which is discussed in Section III-H and Appendix F respectively.

The effect of duty cycle on core loss can be better understood when plotted for different frequencies and flux densities as curves similar to the ones used in datasheets. Fig. 17 shows several of these curves. Duty cycles of 50%, 80%, 85%, and 90% are shown because changes in losses are more significant when the duty cycle is extreme [44] (see Fig. 14b). The effect of duty cycle is far more severe at high frequencies, and, to a lesser extent, at low flux densities (see Fig. 17a), which helps to understand the comparison in Fig. 16b. This high-frequency effect, partly because of the high frequency itself, and partly because of the large duty cycle, is no longer well captured by the Steinmetz equation since losses cannot be solely represented as a power law of frequency (see Fig. 17b). Moreover, the core might start losing permeability at these frequencies.

Waveform shape has only a mild effect on amplitude permeability in this magnetic material. The permeability decreases at all operating conditions when duty cycle is increased from 50% to 80%, in the f and B_{ac} range where measurements are available in both cases. A 4% average drop is found, with a maximum drop of 12% when the peak flux density is large. Since waveform shape does not considerably impact the permeability, sinusoidal measurements might suffice for the characterization of this property.

E. Impact of zero voltage regions

MagNet includes data for trapezoidal B waveforms. To gain information on how zero-voltage regions ($\mathrm{d}B/\mathrm{d}t = 0$)

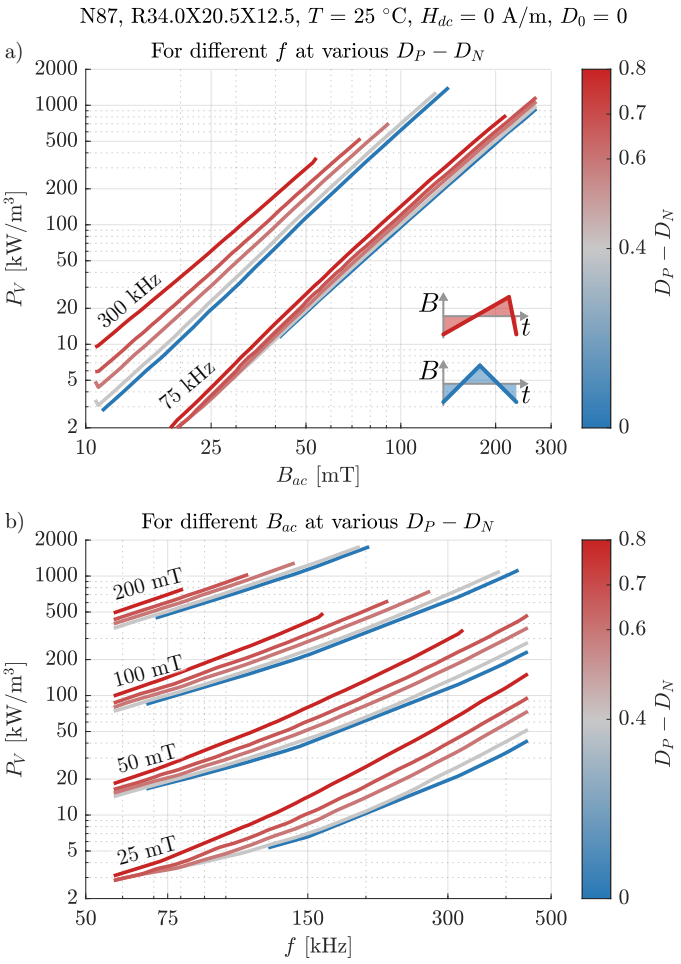

Fig. 17. Core losses as a function of the duty cycle (in color) for a triangular duty cycle excitation at 25 °C and without dc bias. $D_P - D_N$ equal to 0 represents 50% duty cycle triangular waveform while 1 represents a sawtooth waveform. a) For increasing f for different $D_P - D_N$ values b) For increasing values of B_{ac} for a selection of $D_P - D_N$.

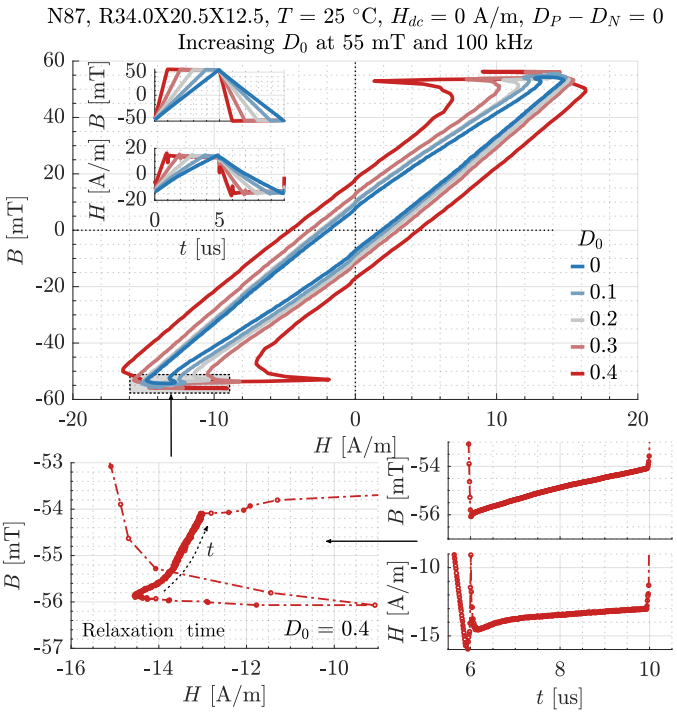

Fig. 18. Measured B–H loops for trapezoidal waveforms of different relaxation time and $\mathrm{d}B/\mathrm{d}t$ at 25 °C, 100 kHz, and 55 mT without dc bias. A zoom of the negative $\mathrm{d}B/\mathrm{d}t \approx 0$ part for $D_0 = 0.4$ on the region where B and H are nearly constant is also included.

impact the B–H loop, measurements where the zero sequence represents different fractions of the total period can be plotted. Fig. 18 shows the measurements for a fixed frequency and flux density amplitude where D_P equals D_N (same rise and fall time), and D_0 is changed (the duty cycle of the region where B is flat). A phenomenon called relaxation impacts the shape of B–H loops. The relaxation phenomena can be observed during the zero-sequences where H decays while B remains nearly constant, shown in the zoom of Fig. 18. It is also observed that the rate of change in H is not constant, but faster at the beginning of the relaxation time. The measurements show the same behavior reported in [30], although longer relaxation times are considered and the effect of switching transitions is negligible in that paper. A description of relaxation processes can be found in [12]. Some models incorporate such effects (see [30], [48] for example), but other models such as the iGSE do not. In this section, this impact is quantified.

The previous figure is not a direct study on the effect of relaxation time, as $\mathrm{d}B/\mathrm{d}t$ during the rise and fall times is changing, and that is responsible for most of the change in the B-H loop. Hence, core losses for different D_0 are not too useful. To study the effect of relaxation on losses, it is convenient to keep $\mathrm{d}B/\mathrm{d}t$ constant while increasing the time the zero voltage regions last. Fig. 19 is included to show the impact of the zero voltage sequences by comparing volumetric losses per cycle and $\mathrm{d}B/\mathrm{d}t$ for a few given B_{ac}, corresponding to waveforms where the frequency is not constant, but rather the $\mathrm{d}B/\mathrm{d}t$ portions of the waveform are constant. It is concluded that the zero voltage sequences negatively impact losses per cycle as expected from relaxation phenomena. Since the input voltage and current have similar levels for a given B_{ac} and $\mathrm{d}B/\mathrm{d}t$, the impact of $\mathrm{d}v/\mathrm{d}t$ in the transitions described in Section III-C is expected to be independent of D_0 here.

Finally, the effect of sections of zero voltage is not significant in μ_a, ranging from -8% to +4%, from the measurements where data is available at 20% rising and falling time with respect to 50% rising and falling time, showing that sinusoidal information can suffice for permeability calculations.

F. Effect of dc bias

The dc bias level of the excitation, a variable that is not fully documented in datasheets, plays a critical role in power magnetics [50]. In this section, the effects of a dc bias in the current in the DUT are analyzed. As mentioned in Section II, H_{dc} is used for comparison, as B_{dc} cannot be inferred with the setup used.

To visualize the impact of dc bias, Fig. 20a shows the measured "$\big(B - \overline{B}\big)$–$H$" loops (since B_{dc} cannot be calculated directly) for 50% duty cycle triangular waveforms at an H_{dc} of 0 A/m, 15 A/m, 30 A/m, and 45 A/m. There is a clear change in permeability with the bias, which can be directly observed

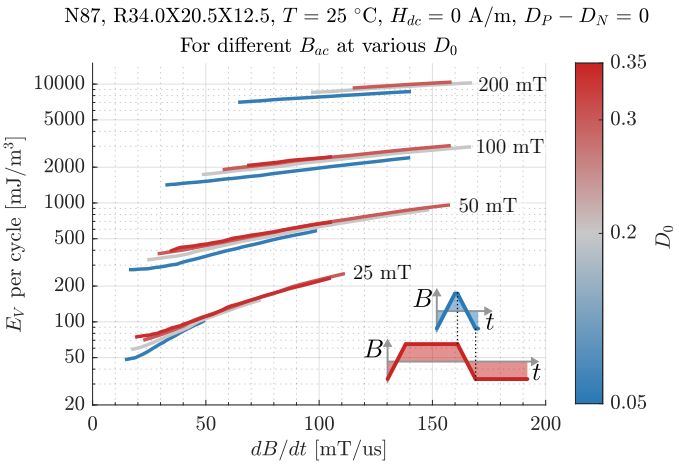

Fig. 19. Energy loss per cycle losses as a function of the duty cycle of the zero-voltage region, D_0, for trapezoidal symmetric excitation at 25 °C and without dc bias as a function of the $\mathrm{d}B/\mathrm{d}t$ of the rising and falling parts of the trapezoidal waveform for given flux densities.

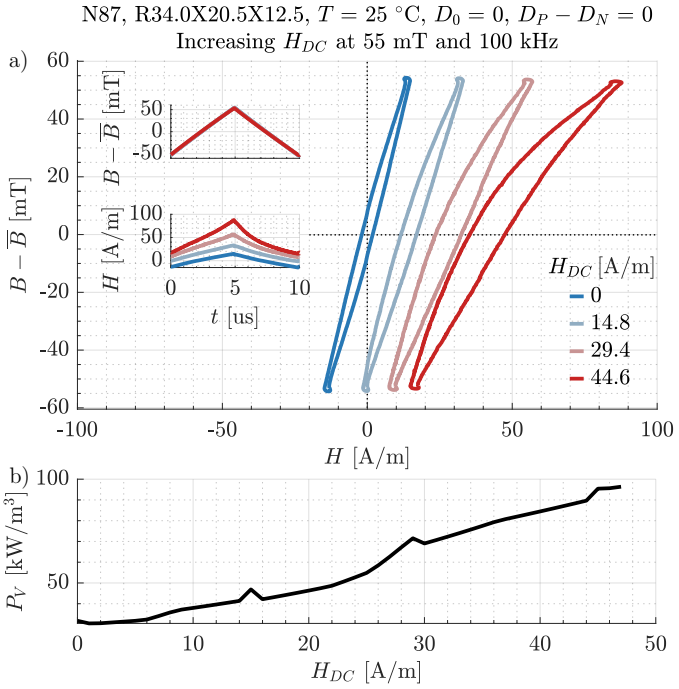

Fig. 20. Triangular 50% duty cycle waveforms at 25 °C, 100 kHz, and 55 mT for different dc bias. a) Measured "$(B - \overline{B})$–H" loops. B_{dc} is not represented as it cannot be directly obtained from the measurements. b) Interpolated core losses as a function of H_{dc} for the aforementioned conditions.

in $H(t)$. Additionally, the bias affects core losses considerably. This increase is quantified in Fig. 20b from a subset of the interpolated losses at different bias levels, frequencies, and flux density amplitudes. Modeling these effects accurately is a pressing need for magnetic component designers.

The literature on the impact of dc bias on core losses is extensive. Early measurements of the impact on dc bias in [50], [51] report the highly nonlinear effects on core losses. A review of the measuring options and effects of the dc bias on core losses is found in [52]. Extensive measurements of the dc bias effect are provided in [43]. Additionally, a model

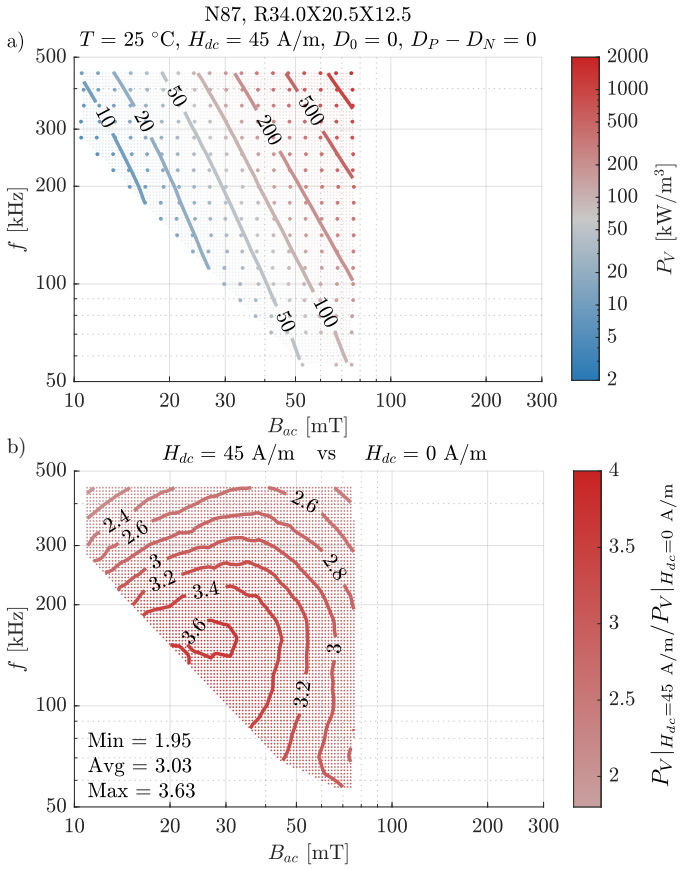

Fig. 21. a) Core losses for a triangular 50% duty cycle excitation at 25 °C and 45 A/m as a function of B_{ac} and f. b) Ratio between losses in a) and without dc bias (Fig. 11). This ratio is referred to as the displacement factor in [54].

is proposed where the dependency of losses with B_{ac} and B_{dc} is first extracted for quasi-static hysteresis, and then modified by a factor that accounts for the frequency and shape of the excitation. The bias has been modeled in Steinmetz-based methods [40], [53], as well as accounted for by modifying the Steinmetz parameters for each H_{dc} [54].

The data in MagNet can be used to evaluate the impact of dc bias on core losses. Fig. 21a shows measurements for triangular waveforms with 50% duty cycle at an H_{dc} of 45 A/m. To avoid saturation, tests at higher B_{ac} are not performed. To be able to draw meaningful conclusions, the ratio between the measurements at 45 A/m and 0 A/m in the f–B_{ac} plane is shown in Fig. 21b. On average, losses increase by a factor of 3 for this specific case, but the interesting feature is that this increment in losses is both frequency- and flux-density-dependent. As discussed in [30], these measurements reveal the limitations of models which decouple the dc bias effect from the frequency effect, such as [40], [43], or models where the dc bias effect is assumed to be independent of the ac excitation, as in [51] (improved in [50]). The conclusion is that the impacts of frequency, flux density, and dc bias are coupled. More sophisticated modeling techniques are needed to obtain accurate predictions of core loss.

To understand the impact of H_{dc} at less extreme cases of bias, a family of curves for different ac flux density and

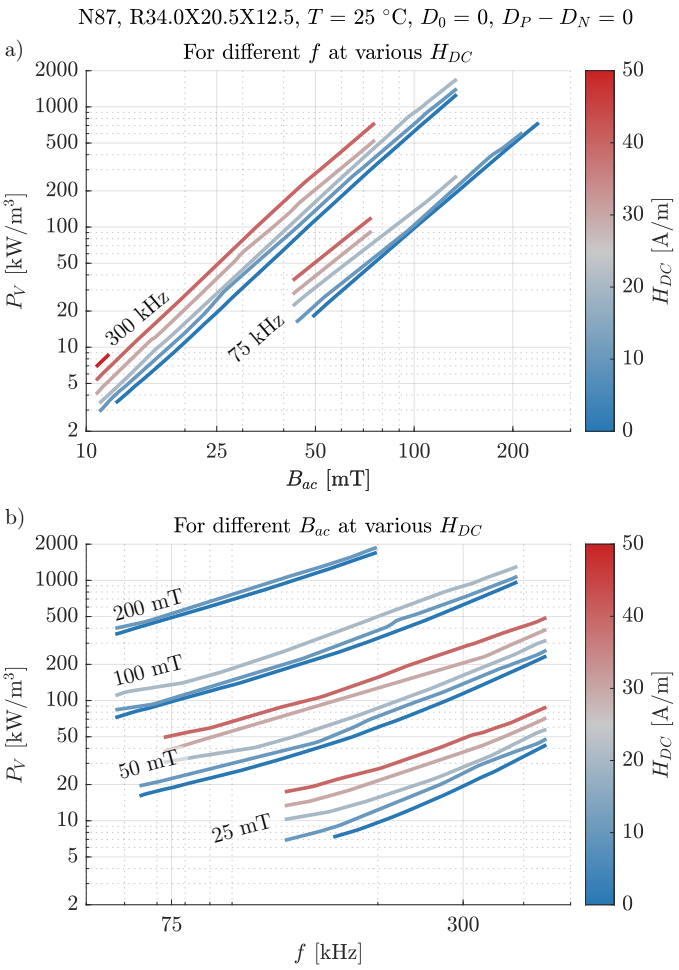

Fig. 22. Core losses as a function of the dc bias for a triangular 50% duty cycle excitation at 25 °C for different H_{dc} values (in color). a) For increasing f for a selection of H_{dc}. b) For increasing values of B_{ac}.

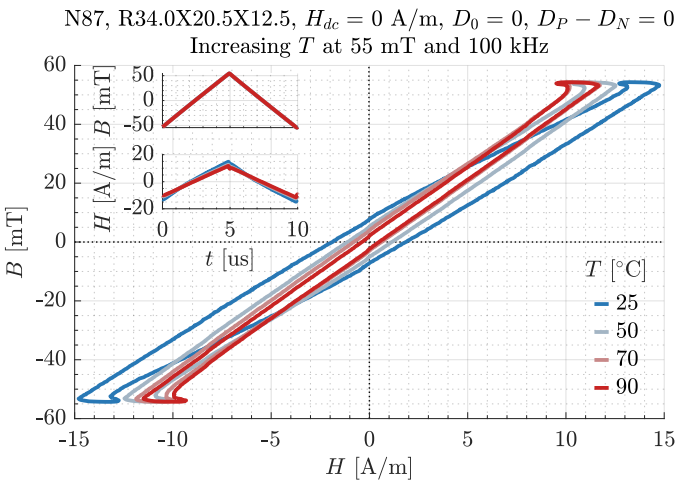

Fig. 23. Measured B–H loops for a triangular 50% duty cycle excitation at without dc bias at 100 kHz and 55 mT for different temperatures.

frequency are shown in Fig. 22 for H_{dc} from 0 A/m to 50 A/m in 10 A/m steps. The core loss curves are moved upward while retaining their shape when bias increases. Designers cannot overlook this effect, and, unfortunately, datasheet information does not cover it.

With a large dc bias, the amplitude permeability generally drops. For the 50% duty cycle triangular data at 25 °C and 45 A/m dc bias (about 250 mT if a relative permeability of 4400 is used to relate H_{dc} with B_{dc}), the relative amplitude permeability is around 1000, a substantial decrease compared with the results without dc bias in Fig. 12. It yields a ratio $\mu_a|_{H_{dc}=45\ \mathrm{A/m}}/\mu_a|_{H_{dc}=0\ \mathrm{A/m}}$ of 0.4±0.03, changing slightly in different regions of the f–B_{ac} plane. The effect is fairly constant across frequency and peak flux density, although the latter may be due to the small range of ac flux density tested (from 10 mT to 80 mT in this case).

G. Temperature dependence

Core loss is also affected by external factors such as temperature because, among other reasons, permeability, permittivity, and conductivity are temperature-dependent [9]. The B–H characteristic is affected by temperature, as reported in datasheets for quasi-static conditions (see Fig.1a). For low frequencies, B–H loop variations with temperature are studied in [55], and a model for the saturation with temperature is proposed in [21]. B–H loops are shown in Fig. 23 for 25 °C, 50 °C, 70 °C, and 90 °C for 50% duty cycle triangular waveforms. In this temperature range, it can be observed how losses decrease with temperature while amplitude permeability increases for this magnetic material, with changes being more significant at lower temperatures. There are materials available in the market to suit specific needs: reasonable temperature stability, losses nearly constant across wide temperature ranges, minimum losses at specific temperatures, and so on. N87 is a material with minimum losses around 90-100 °C.

Fig. 1d already shows how temperature impacts core losses; however, for this specific material, the datasheet only provides data at 100 kHz. Although more data can be found in the manufacturer's software [11], data is only available for sinusoidal waveforms and without dc bias. The effect of temperature on losses has been typically addressed by providing different Steinmetz parameters at different temperatures, or by modifying methods to add the temperature dependence [47]. Fig. 24a shows the measured core losses at 90 °C for 50% duty cycle triangular waveforms for the N87 material while Fig. 24b depicts the variation with respect to the results at 25 °. At high frequencies and low flux densities, the behavior reverses and core losses increase when the temperature is increased. The effect of temperature is both frequency- and flux-density-dependent and explains why α and β are specified for different temperatures.

The effect of temperature is better understood with several core loss lines plotted for different temperatures (Fig. 25). As expected from the datasheet information (Fig. 1c), temperature changes have a greater impact on losses at low frequencies. The information on the datasheet, even though far more complete regarding temperature as compared to other parameters, might not suffice to cover the full relationship between P_V, T, f, and B_{ac}.

Permeability is also affected by temperature, not only the initial permeability but also the amplitude permeability, as

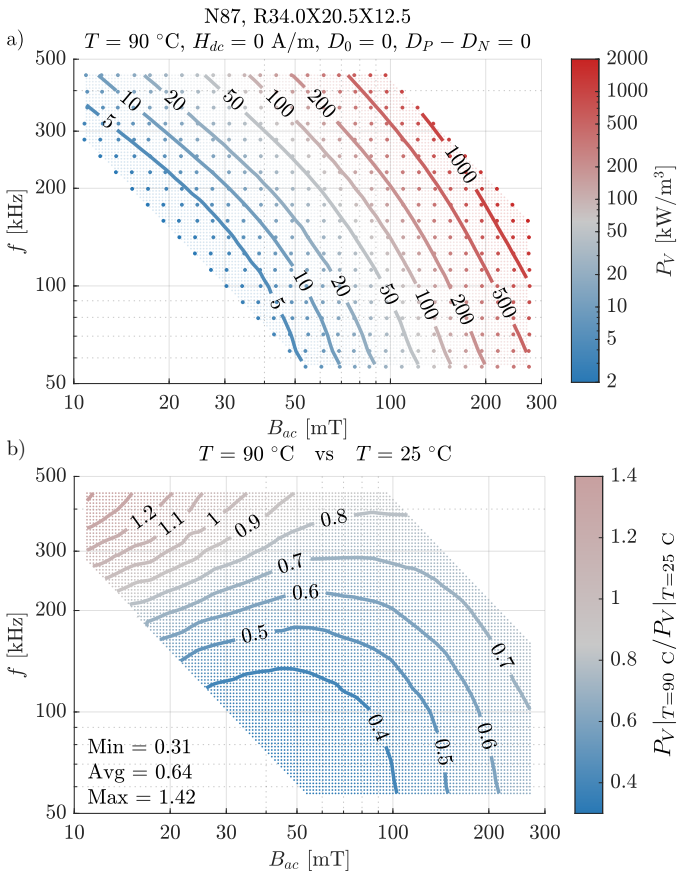

Fig. 24. a) Core losses for a triangular 50% duty cycle excitation without dc bias at 90 °C as a function of B_{ac} and f, for comparison with the data in Fig. 11 at 25 °C. b) Ratio between the volumetric core loss at 90 °C and 25 °C.

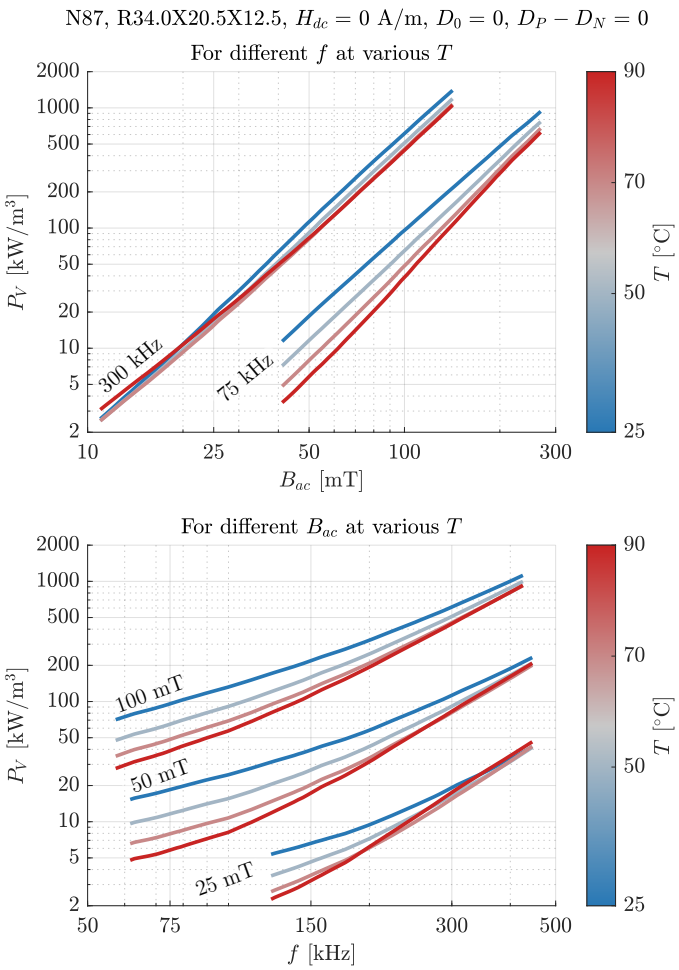

Fig. 25. Core losses as a function of the temperature for a triangular 50% duty cycle excitation without dc bias. a) As a function of frequency for different B_{ac}. b) As a function of B_{ac} for a set of frequencies.

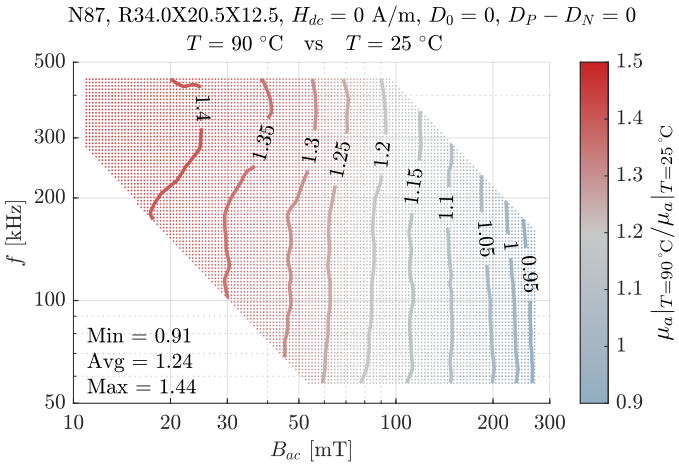

Fig. 26. Ratio between the amplitude permeability at 90 °C and 25 °C for 50% duty cycle triangular excitations without dc bias, as a function of B_{ac} and f. The amplitude permeability at 25 °C is shown in Fig. 12.

shown in Fig. 1b. Fig. 26 shows the ratio between the permeability at 90 °C and 25 °C for 50% duty cycle triangular waveform measurements. It agrees with the μ_a reported in Fig. 1b even though triangular data is used instead of sinusoidal data. From this plot, it is clear that the permeability increases with temperature, and the change is heavily influenced by peak flux density. For N87 material, frequency and temperature are nearly independent factors.

H. Core size impact

The magnitude of the magnetic field is not constant inside the core. For instance, in toroids, the field is stronger in the inner radius than in the outer radius of the core. In addition, ferrites properties are not homogeneous for large cores because of firing/sintering processes [37]. Besides the variability in magnetic properties and the frequency-independent effect, skin-effect and dimensional resonances also modify the magnetic field distribution in the core. These phenomena are related to the propagation of electromagnetic waves inside the core due to the high permeability and permittivity. They become significant at higher frequencies and depend on the dimensions of the core [8], [13], [14], [37], [56]. A description of the physics behind these phenomena can be found in [12], but these effects are difficult to quantify because manufacturers do not provide adequate information on the electrical properties of the core [8]. Models for the flux density distribution based on measurements of the electrical properties of the core are available in [13].

Several different sizes of toroids have been measured under

TABLE I
N87 CORES USED TO EVALUATE THE EFFECT OF CORE GEOMETRIES

TDK's denomination	h [mm]	$\frac{d_a-d_i}{2}$ [mm]	l_e [mm]	A_e [mm^2]	V_e [mm^3]	N
R58.3×40.8×17.6	17.6	**8.75**	152.4	152.4	23230	5
R34.0×20.5×12.5	12.5	**6.75**	82.06	82.60	6778	5
R25.3×14.8×10.0	10.0	**5.25**	60.07	51.26	3079	8
R16.0×9.6×6.3	6.30	**3.20**	38.52	19.73	760	14

the same conditions employing the setup used to collect the data in MagNet (see Section II-A) to provide an estimate of the magnitude of effect that core size has on magnetic properties. The onset of these effects is dominated by the smaller of the two dimensions across the core area [13]. For toroids, this is either height h or external radius minus internal radius $(d_a - d_i)/2$. In this section, the results for 50% triangular waveforms at 25 °C without dc bias are discussed for the toroids listed in Table I. In all cases, the smaller length is $(d_a - d_i)/2$, marked in the table.

Even though B and H depend on the position in the core, their "scalar values", calculated based on effective dimensions, are still a powerful way to understand and compare magnetics. B–H loops in similar B_{ac} conditions at 500 kHz, the highest frequency tested, are shown in Fig. 27 for the core listed in Table I. Significant differences among the B–H loops are observed that cannot be attributed to small changes in the excitation, $\mathrm{d}v/\mathrm{d}t$, or temperature changes. For instance, at this specific operation point, the volumetric loss in the large core is 32.4 kW/m^3 while the small core has only 26.3 kW/m^3. Relative amplitude permeability drops from 2800 in the small core to 2400 in the large core. However, this data must be read carefully, as tolerances in the core create variations on these numbers on the same order of magnitude, as reported in Appendix G.

The skin effect and dimensional resonances have different repercussions on core losses depending on the geometry, size, permeability, conductivity, and permittivity of the core [9], [42]. Moreover, as discussed in [42], dielectric losses depend on core geometry and size. Yet, core losses are typically provided only for a given shape (R34.0×20.5×12.5 in the datasheet for N87 [10]). The measured losses, as a function of f and B_{ac}, are shown in Fig. 28. The variation, although small, is more significant than the expected error in the measurement (see the Appendix) showing that the size of the core impacts core losses. For instance, the ratio between the core loss of the large core with respect to the small core in the range where measurements are available in both cases is, on average, 1.16, with a maximum value of 1.31 at 500 kHz.

Similarly, amplitude permeability is also impacted. $\mu_a|_{\mathrm{R58.3\times40.8\times17.6}}/\mu_a|_{\mathrm{R16\times9.6\times6.3}}$ is 0.88 on average, almost equal at low frequency and high flux density but with a minimum of 0.85 at 500 kHz. From these results, it is concluded that considering the magnetic properties only to be a function of the material can be a misleading approach when deriving accurate models. This is problematic since the frequency/size at which this geometry-dependent phenomenon starts is not determined yet due to the lack

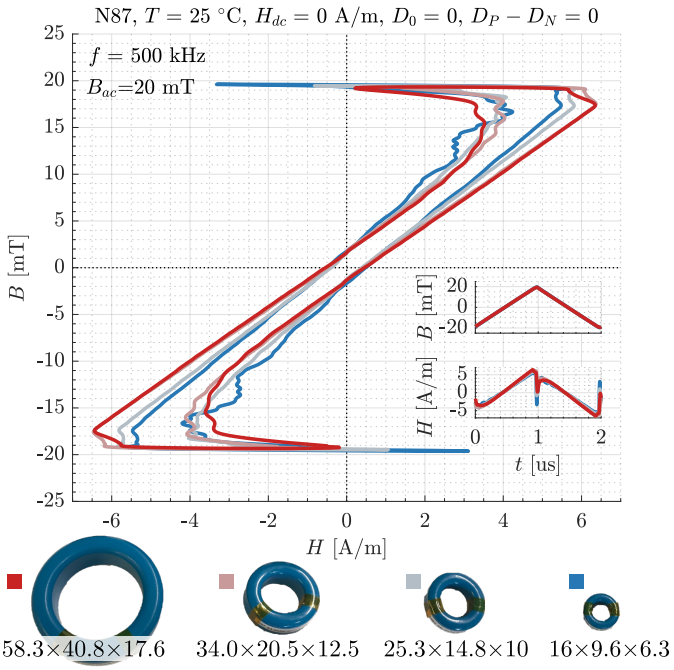

Fig. 27. Measured B–H loops at 50% duty cycle 25 °C, 500 kHz, and nearly 20 mT without dc bias for different core geometries. Small differences in H_{dc} are removed to make the comparison easier.

of data [8]. Providing a frequency range for each material is not enough, and the frequency range, core losses, and permeability should be specified for each combination of core and shape instead of being assumed as shape- and size-independent.

I. Material impact

In this paper, the properties of Mn-Zn soft ferrites are discussed using the material N87 as an example but each material has its unique properties, hence distinct B–H loops. Fig. 29 shows the core loss with 50% triangular excitation of several Mn-Zn ferrites from different manufacturers. One should read these plots carefully since the impact of geometry can skew the results favoring one material or another as they are not measured for the same dimensions. This graph also illustrates the relative importance that operating conditions (such as dc bias or geometry) can have over the selection of the proper material. It is beyond the scope of this paper to investigate how the variation of magnetic properties is impacted by different parameters for all materials, but the data can be found in the MagNet database.

IV. Feasibility of Models with Decoupled Factors

The goal of this section is to find whether different effects can be decoupled from one another based on the collected data. Since there is a relatively large variation from core to core (see Appendix G), only results for a single core are provided and the effect of geometry is not discussed. As noted in Section III-C, the effect of $\mathrm{d}v/\mathrm{d}t$ cannot be eliminated and might distort this analysis; so do small variations in temperature discussed in Appendix E. Additionally, an important parameter

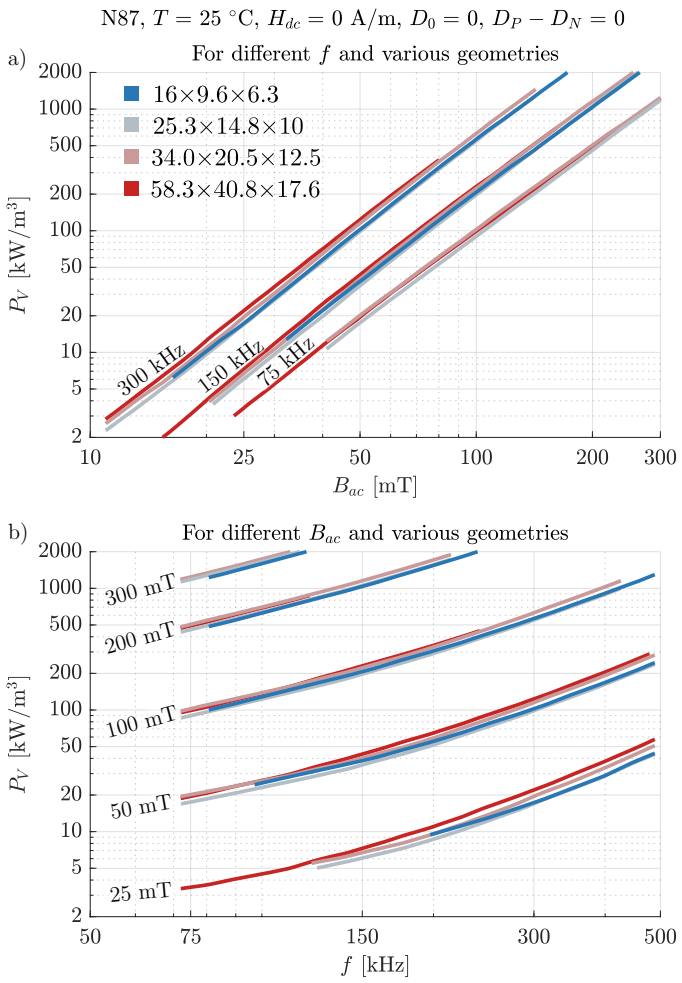

Fig. 28. Core losses for different geometries of the N87 toroids for a triangular 50% duty cycle excitation without dc bias at 25 °C. a) As a function of frequency for different B_{ac}. b) As a function of B_{ac} for a set of frequencies.

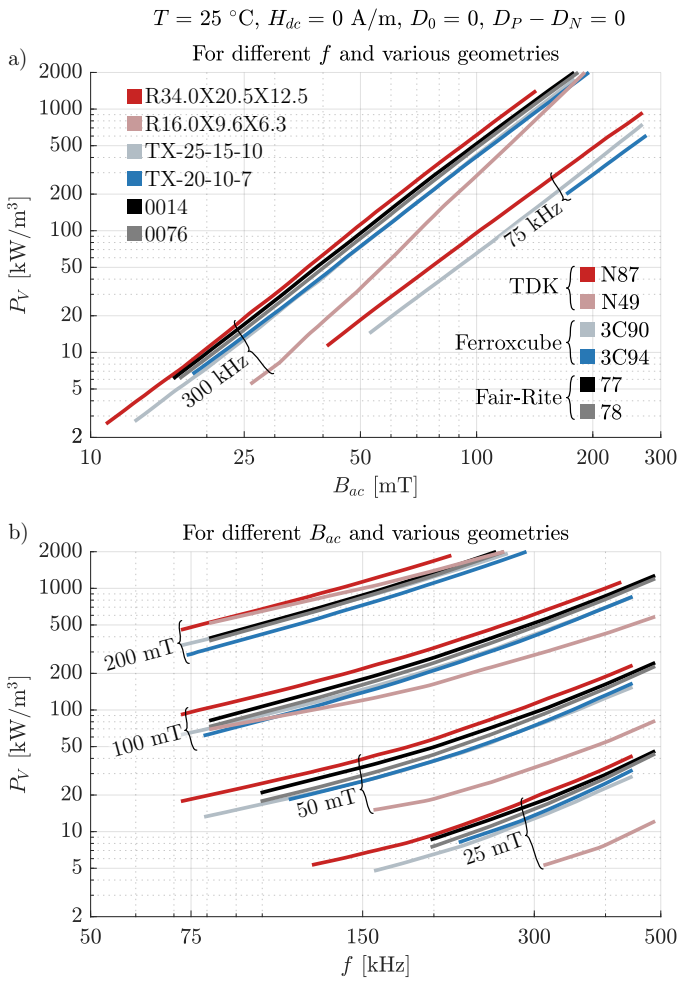

Fig. 29. Core losses for different Mn-Zn materials for a triangular 50% duty cycle excitation without dc bias at 25 °C. a) As a function of frequency for different B_{ac}. b) As a function of B_{ac} for a set of frequencies.

affecting core loss not discussed in this work is the mechanical pressure applied to the core [9].

Traditionally, the effects of frequency and flux density have been modeled as independent of each other. For example, according to the Steinmetz equation, $P_V|_{B_{ac1}}/P_V|_{B_{ac2}}$ is a function of B_{ac1} and B_{ac2} but not of frequency (holding all other conditions constant). Similarly, form the Steinmetz equation $P_V|_{f_1}/P_V|_{f_2}$ is related by the factor α, which might depend on f slightly but should not depend on B_{ac}. This is valid to a large extent; for instance, in Fig. 11b, the ratio $P_V|_{B_{ac1}}/P_V|_{B_{ac2}}$ (which is the slope of $P_V(B_{ac})$) does not considerably change for different frequencies. Similarly, from Fig. 11c, the slope of the $P_V(B_{ac})$ curves is similar for different flux densities (although the slope changes with frequency).

It is important to know to which extent the effect on losses of other parameters (temperature, dc bias, or duty cycle) are independent of one another. Equations in the form of $P_V(B_{ac}, f, H_{dc}, D, T) = k \cdot f(B_{ac}) \cdot f(f) \cdot f(H_{dc}) \cdot f(D) \cdot f(T)$ where each contribution adds a multiplicative factor are unlikely valid. To check which factors can be linked to and decoupled from others, the ratio between power losses under different conditions is examined. For instance, Fig. 30 shows the variation of losses from 50% to 80% duty cycle at 90 °C. In this case, $P_V|_{D_1}/P_V|_{D_2}$ clearly depends on the frequency or peak flux density considered. Furthermore, we can see an additional layer of complexity by comparing Fig. 30 to Fig. 16b which shows the same ratio, but for 25 °C. $P_V|_{D_1}/P_V|_{D_2}$ is temperature-dependent (the ratio is different in both plots). This is expected given the fact that temperature affects the impact of frequency and flux density on core loss.

Similarly, the effects of temperature and dc bias are heavily coupled. Fig. 31 shows the ratio of P_V at 45 A/m dc and 0 A/m at 90 °C. Please compare this figure to Fig. 21b, which depicts the same ratio at 25 °C. Not only in value (for instance, the average increase in losses at 25 °C is 200% while at 90 °C is 100%) but trends are heavily affected. Therefore, the effect of H_{dc} on losses is significantly influenced by f and B_{ac}. In [50], the increase of losses because of dc bias is found to be frequency- and geometry-dependent at low flux densities.

The coupled effect of duty cycle and dc bias is observed by comparing $P_V|_{D_P=80\%}/P_V|_{D_P=50\%}$ at 45 A/m in Fig. 32 with the results at 0 A/m in Fig. 16b. Again, although the relation with respect to B_{ac} and f is similar, the maximum

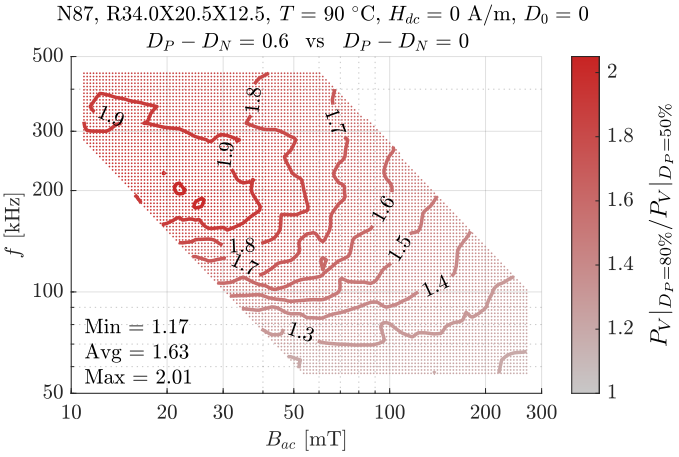

Fig. 30. Ratio between P_V at 80% duty cycle and 50% duty cycle at 90 °C. Please compare with the data at 25 °C in Fig. 16b.

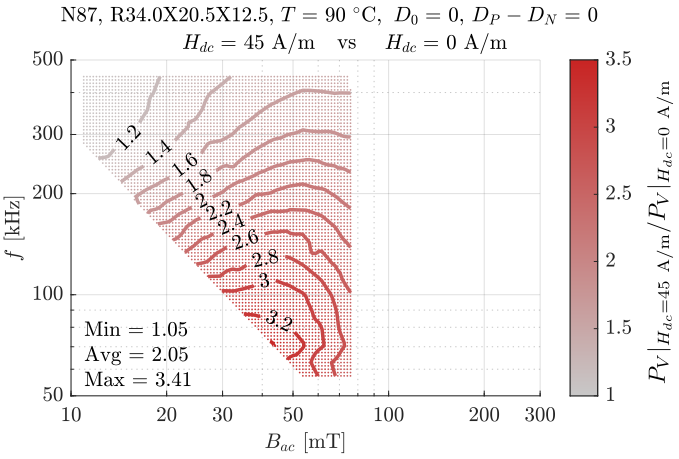

Fig. 31. Ratio between P_V at 45 A/m and 0 A/m dc bias at 90 °C. Please compare with the data at 25 °C in Fig. 21b.

variation at 0 A/m is 2.05 while the maximum variation at 45 A/m is only 1.67. This difference could not be accounted for by models treating the effect of dc bias to be independent of the effect of duty cycle, for a given frequency, peak flux density, and temperature.

From the measurements, $P_V(B_{ac}, f, H_{dc}, D, T)$ cannot be decoupled into any set of multiplicative factors dependent on different parameters when high accuracy is expected across a wide range of operating conditions. Please note that the measurements are subject to errors and the temperature stability should be further improved as detailed in the Appendix, but it is unlikely for measurement errors to give rise to flawed overall trends. Note that this analysis does not advise against loss separation models where different contributions to losses are added up and each of the contributions is a function of a few parameters (for instance, the static hysteresis contribution being independent of waveform shape or frequency). This work advises against unified models where any additional variable (bias for instance) acts as a factor modifying the total losses. Eventually, to obtain satisfactory models for any waveform shape, losses should be defined as $P_V(t) = f(B(t), T)$, from which special cases (steady state

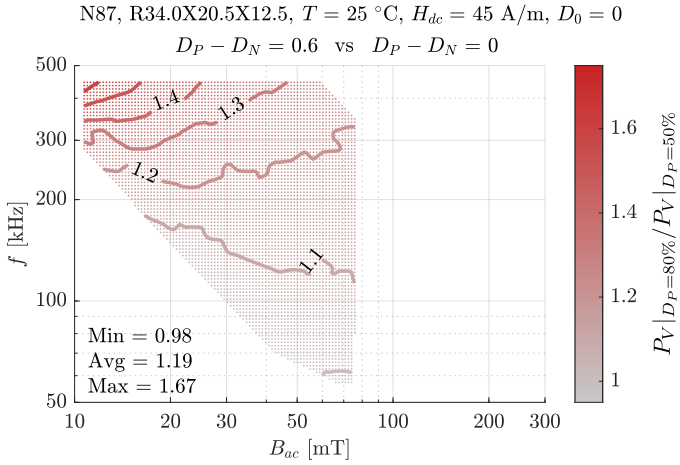

Fig. 32. Ratio between P_V at 80% and 50% duty cycle at 45 A/m. The range is limited to the frequencies and flux densities where data is available for both duty cycles. Please compare with the data at 0 A/m in Fig. 16b.

operation or triangular waveforms without bias as examples) could be derived, and then described as a function of desired parameters (e.g., frequency and duty cycle). A further step would be to have models where the uneven distribution of $B(t)$ in different parts of the core is accounted for, hence having models depending on the geometry of the core.

Intricate empirical models could be proposed as a solution, but complex models are hardly going to be adopted by designers and are likely to be difficult or unstable to parameterize. Empirical solutions parameterized with subsets of data can be a reasonable framework, but extrapolation to other operating conditions should be avoided. In general, models capturing the impact of individual factors may provide useful guidelines to the design process, but may not accurately describe the material behaviors when many factors co-exist. Extensive datasets to create loss maps and direct interpolation might also be applied. Sadly, the available measurements from manufacturers do not cover all realistic operation scenarios. Better physics-based models are likely to improve the accuracy of the predictions and point other models in the right direction, but usually, pushing research forward needs experiments where some of the effects can be safely neglected. Integrating models which account for different phenomena can be complex in the end, bringing us again to the intricate and hard-to-use models. Finally, machine learning techniques such as neural networks can be employed to model core loss accounting for all desired parameters, yet again, accurate and extensive datasets are needed for training. Neural networks in this framework can be considered as a form of efficient interpolation of the data, where the information is stored in the structured weights and biases of the network rather than data points. Challenges with machine learning models include compatibility and integration with existing tools, and difficulties with generalizations to scenarios different from the test data set.

V. Conclusions

In this work, the data in MagNet has been employed to explain and quantify the challenges power magnetics modeling

has to overcome. Extensive B–H loop, core loss, and permeability data have been analyzed to illustrate how peak flux density, frequency, waveform shape, dc bias, temperature, core size, and core material impact the behavior of the magnetic core. This analysis supports the results of other researchers where each of these factors or a few factors are studied in detail, but brings an additional challenge: studying each parameter affecting the core B–H loop independently is not the best approach to follow, as these effects are intertwined. For this reason, it is difficult to make a simple yet accurate model for magnetic materials valid in a wide range of operating conditions. Machine learning models such as neural networks can capture the effect of the different parameters with reasonable accuracy if a reliable dataset covering the range of operating conditions and waveforms that are of interest is available for training. In a separate paper [16], we provide examples of neural networks architectures capable of modeling B–H loops and core losses under the operating conditions covered in this work (excluding the impact of $\mathrm{d}v/\mathrm{d}t$ or core size) with data in MagNet [17].

APPENDIX
DETAILED ERROR ANALYSIS

Understanding the sources of error is a necessary step to ensure the accuracy and validity of the B–H measurements [20]. In this appendix, the procedure to obtain the different errors in the setup and their sources are described. Similar discussions can be found in [20], [54], [57] for their respective setups using the V-I method. All the problems have been tackled to the extent possible, yet the data is not error-free. Besides the errors reported here, data processing can introduce additional errors. These errors strongly depend on the accuracy of the frequency detection algorithm. Please note that since errors are heavily influenced by the test conditions, a single number to provide accuracy is not representative of the complete dataset. In this section, the error is shown for the measurements of the N87 material with 50% triangular waveform at 25 °C without dc bias, but similar error maps can be created for each operating condition and material in the MagNet database.

A. Effect of phase delay

A known problem of the two-winding method is the effect of phase mismatch between the voltage and current measurements. Since reactive power is much larger than average power, a small phase shift can cause a large error in loss estimation. This error is regarded as the main limitation of this method when it comes to high-frequency measurements [20], [25], [27], [52], [58]. Since the parasitic capacitance and inductance in the shunt are not expected to be a problem in the considered frequency range [20] and the delay between two channels in the oscilloscope is negligible ($\leq$100 ps), the most significant source of error in this setup is credited the different delays caused by the unmatched length of the probes. A delay of 1.6 ns has been measured (0.3° at 500 kHz for reference) by comparing the current measurement with the voltage probe when measuring the same current. This delay is not compensated. Other sources of delay are listed in [20].

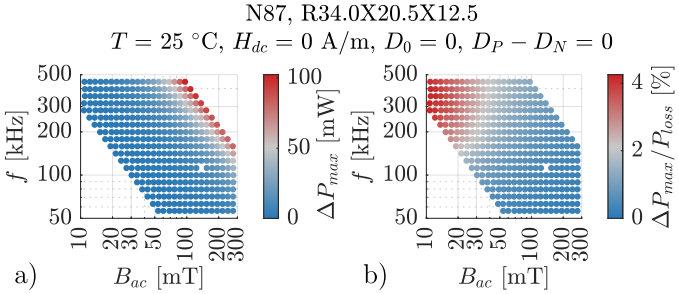

Fig. 33. Effect of 1.6 ns maximum delay between the voltage and current measurement on a subset of the N87 data. a) Worst case added or subtracted losses. b) Relative error.

The effect of delays in the measurements for sinusoidal waveforms is explained as an additional phase shift because of the delay on top of the phase shift caused by the restive behavior of losses [58]. For simplicity, the worst-case absolute error is analyzed here. This is the case for a lossless inductor. The discrepancy in power for a sinusoidal voltage of amplitude V and sinusoidal current of amplitude I shifted and t_{delay} with respect to the ideal 90° and simplified using the small-angle approximation is given by:

$$\Delta P_{max} \approx V \cdot I \cdot |t_{delay}| \cdot \pi \cdot f \tag{6}$$

This simple equation relates the frequency, reactive power $S = V \cdot I/2$, and time delay with the error in losses. ΔP_{max} increases with frequency and results in large relative errors for materials/operation points where the quality factor is high.

This approximation can be used to obtain the worst-case variation in losses for PWM waveforms as well. In essence, the delay in current causes a discrepancy in the average current in each one of the switching states. This variation in current multiplied by the applied voltage gives rise to active power. As long as $t_{delay} \ll d \cdot T$, on a first approximation, for trapezoidal symmetric and triangular waveforms of any duty cycle this variation in measured loss is given by:

$$\Delta P_{max} \approx V_{in} \cdot I_{pk} \cdot |t_{delay}| \cdot 4 \cdot f \tag{7}$$

As an example, the error due to a delay of 1.6 ns can be estimated for triangular 50 % duty cycle waveforms at 25 °C without dc bias (the data shown in Fig. 11) by considering the measured voltages and currents waveforms as those of a lossless inductor and using Eq. (7). This worst-case error in the measured losses is shown in Fig. 33a. Even though the error in losses is significantly higher with increasing f and B_{ac}, so do the measured losses. As a result, the relative error not only depends on frequency but also on the quality factor of the operation point, as shown in Fig. 33b. The relative error due to the phase shift is below 5% for N87, but a higher relative error would be obtained for low-loss materials and higher frequencies (24% in the worst operation point for N49 for the 50% triangular data in MagNet for instance).

B. Effect of probes and oscilloscope error

The probes and oscilloscope add up errors because of changes in gain, offset, and vertical resolution. These errors

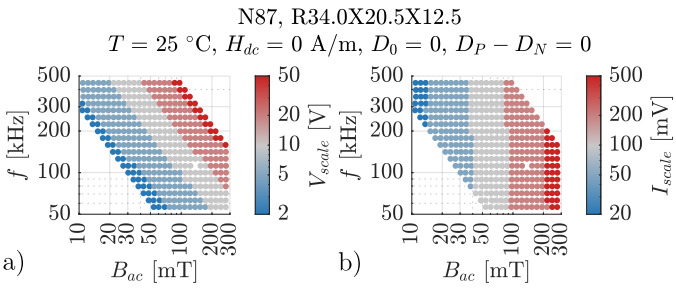

Fig. 34. Scale for the voltage and current used for the tests for triangular 50% duty cycle waveforms at 25 °C without dc bias measurements.

depend on the vertical scale used to capture the data. The voltage and current vertical scales are [0.5, 1, 2, 5, 10, 20, 50] V and [0.01, 0.02, 0.05, 0.1, 0.2, 0.5, 1] V respectively (the current is measured using a 0.964 Ω equivalent resistance). A 40% margin is left between the maximum value of the signal and the maximum value the oscilloscope can read to avoid clipping. The vertical scales used for the measurements for the subset of data are shown in Fig. 34 to clarify the oscilloscope setup.

The gain error between samples is specified as a constant part, the dc gain accuracy, which is ±1.5% for the Tektronix DPO4054, and a variable part, which is 0.15 times the volt per division used. Therefore larger vertical scales imply higher absolute error. On top of that, there is a constant 1.2 mV error in each channel. This equation is used to calculate peak-to-peak error in the oscilloscope based on the technical reference [59] and it is considered as a basis for this analysis, although real errors are probably not so large. Moreover, the passive probe P6139A has ±0.5% attenuation and the accuracy of the shunt resistor (T&M Research W-5-10-1STUD) is ±0.2%. The total worst-case relative error added by the scope and probes is shown in Fig. 35 a-c, in the voltage measurement, the current measurement, and in the loss calculation, respectively. A fixed 3.7% error is the result of the dc gain accuracy and probes errors and tolerances. The constant 1.2 mV factor mostly deteriorates data at low currents (up to 1%). Most of the error is related to the vertical scale selected, up to 5% because of the voltage near the change of vertical scale region from 2 V to 5 V or 20 V to 50 V and other 5% near the change from 20 mV to 50 mV and 200 mV to 500 mV for the current measurement. The error distribution follows a pattern mostly dictated by the changes in the vertical scale. Please note that this is the worst-case error, the distribution of the error is unknown and it is very unlikely that all the errors add up in both voltage and current measurements at the same time as in the plot. The expected error is discussed in Appendix F. A better oscilloscope could lead to more accurate results. A limitation of the dc bias measurement is that the scale for the current remains large even for low I_{ac} due to the large I_{dc}, leading to lower accuracy at larger dc bias. Also, note that the error on the voltage measurement directly affects the reported B_{ac}.

Regarding the offset error, since the average voltage is removed from the measurement during data processing, it does not pose a problem. However, the offset in the current

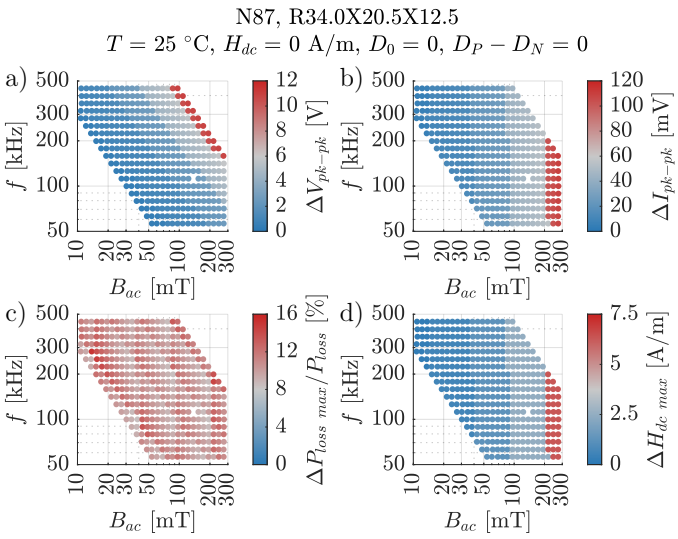

Fig. 35. Effect of the gain and offset errors in the measurements of N87 triangular 50% waveforms at 25 °C without DC bias. a) Worst-case error because of the passive probe and scope in the peak-to-peak voltage measurement. b) Worst-case error because of the passive probe and scope in the peak-to-peak current measurement. c) Worst-case relative error in the core loss; calculated as $\left(V_{pk-pk} + \Delta V_{pk-pk}\right) \cdot \left(I_{pk-pk} + \Delta I_{pk-pk}\right) / \left(V_{pk-pk} \cdot I_{pk-pk}\right)$. d) Worst-case absolute error due to offset in the dc bias.

measurement affects H_{dc}. The offset error is 0.2 of the selected vertical scale. The error, in absolute terms, is shown in Fig. 35d for the current scale shown in Fig. 34b, translated to H for convenience. The maximum error reaches about 6 A/m.

The random noise is not expected to affect measurements and it is mostly removed by the 20 MHz filter in the oscilloscope. The error of this filter is considered negligible as the fundamental frequency of the excitations is limited to 500 kHz. Tests without the filter show negligible variation in core loss.

The last concern when using an oscilloscope to collect data is the effect of the vertical and horizontal resolution. The number of bits for the vertical resolution (8 bits with this scope) and the number of samples (800 ps sampling time and averaging every 10 samples) can limit the accuracy of the B–H loop. Fortunately, the effects on permeability or loss calculation are not significant. For illustration, Fig. 36 shows one of the measured loops subjected to additional heavy downsampling. P_V or μ_a is not too affected even in such extreme conditions, although results can change from point to point. In general, the measurements are not affected much by sampling effects at this level. B is less prone to error compared to H as it results from the integration of the voltage. Moreover, the single-cycle algorithm considerably reduces the effects of downsampling, both in the horizontal and vertical scales. Since the average of several switching cycles is used, the resulting waveform is averaged out. As a result, the resolution is not expected to cause a significant error in these measurements.

C. *Effect of parasitic elements in the circuit*

There are several parasitic elements affecting the measurements [27]. Since a secondary winding is used for voltage measurements, the effect of winding resistance and leakage inductance (both in primary and secondary) can be safely

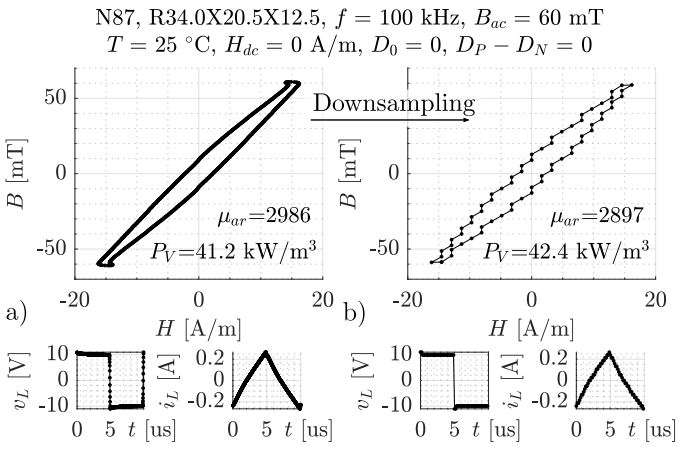

Fig. 36. B–H loops for one of the measured waveforms with the values of amplitude permeability and core loss calculated from the B and H signals. a) Measured B–H loop. b) Downsampling the number of points per cycle from 1024 to 64 and rounding V and I to one-tenth of their respective peak-to-peak values. The effect on losses and permeability is not so significant even in such an extreme case.

neglected. The input resistance of the passive probe is large enough (10 MΩ) so the current can be neglected. However, any capacitive element in parallel with the DUT can impair the current measurement. This includes the parasitic capacitance of the primary winding, the capacitance of the secondary winding, the parasitic capacitance of the passive probe (8.0 pF) (which is reflected in primary), and any additional capacitance from the leads connecting the device to the shunt. Note that the capacitance of the winding is larger when submerged in oil as compared to air. When a sinusoidal voltage is applied, the current through this parasitic capacitance is nearly 180° shifted with respect to the DUT current, and, as a result, the measured current has a lower amplitude than the real value. As a reference, for 500 kHz and 70 µH, a ∼70 pF in parallel with the DUT would cause a 5% variation in the current measurement. For PWM waveforms, the effect is a large current through the capacitor during the $\mathrm{d}v/\mathrm{d}t$ region. Then, the measured current in the shunt shows a dip during the transition depending on the transition speed which is not caused by the behavior of the core solely as discussed in Section III-C.

The second source of error is the parasitic elements in the current measurement circuit. Any inductance or capacitance in the shunt resistor would change the measured voltage. Nevertheless, these effects can be disregarded as the bandpass frequency of the selected shunt is 800 MHz. The parasitic capacitance of the BNC connector for the shunt is lower than 10 pF. Besides the capacitance of the shunt itself, the primary-to-secondary capacitance of the DUT has a similar effect, as it can be considered to be connected across the shunt (grounded in secondary through the passive probe) as a worst case. This capacitance phase shifts the current measurement. For the DUT, a 25 pF primary to secondary capacitance is measured when submerged in oil. Considering a 1 Ω shunt measuring a sinusoidal current at 500 kHz, this capacitance creates an additional 0.044° phase shift, negligible compared to the 0.3° phase shift because of the probes.

D. Non-ideal excitations

Any low-frequency oscillation changing the voltage or current measurement from one cycle to the next can cause additional errors. This error is evaluated during the data processing stage and rogue data is removed. Secondly, note that waveforms are not as ideal as listed. Sinusoidal waveforms can be slightly distorted (and THD is calculated as a measure to address its quality), and triangular and trapezoidal waveforms do not have perfect edges. Hard switching (or partial or incomplete ZVS) leads to different current waveforms during the transition depending on the frequency and voltage of the excitation. For instance, for 10% duty cycle at 500 kHz, the dead time (70 ns) is comparable with D_P/f (200 ns). Additionally, the control times can only be set as an integer number of clock cycles, so exact frequencies and duty cycles are not always attainable. Finally, the shunt and parasitic resistances make the impedance of the load not purely inductive, creating a voltage drop that can distort the voltage excitation. Note that this is not a problem for the calculations but rather for how data is reported, because B and H are directly obtained from the measurements.

E. Effect of the variation in temperature during testing

Due to the average losses during the continuous swapping of operation points, the temperature in the core may rise even with the core submerged in an oil tank at a controlled temperature (see Section II-A). This small temperature change can have a subsequent impact on losses. For instance, the temperature of the core right after a set of tests for triangular 25 °C no dc bias measurements for all frequencies and flux densities, which takes about 15 min, was 30 °C (using a thermal camera). This 5 °C variation in reported temperature has an impact on losses. Moreover, at 90 °C water temperature, the oil temperature is slightly lower (87 °C), also affecting the quality of the data. The temperature profile of the core during testing is not known as the core is submerged in oil. A complete analysis of the maximum variation between the set temperature and the external temperature of the core is yet to be done and further improvements such as adding a waiting time between tests, or measuring the core temperature could help mitigate this issue.

F. Assessing reproducibility

One of the main drawbacks of inferring B from v_L is that the initial magnetization of the core is unknown. The voltage is only captured after the core has been excited for a short amount of time once steady state operation has been reached (∼0.5 s). This is a fundamental limitation and can be challenging as the history of $B(t)$ impacts the subsequent B waveform. Fortunately, accommodation reduces the impact of the magnetic history with the number of switching cycles [19], [60]. Moreover, a demagnetization sequence is briefly applied after the test at the highest B_{ac} for each frequency. Therefore, it is reasonable to expect similar results in the measurements regardless of the initial B_0 before the excitation is applied.

To validate the reproducibility of the measurement, the set of tests at 25 °C without dc bias for 50% duty cycle triangular

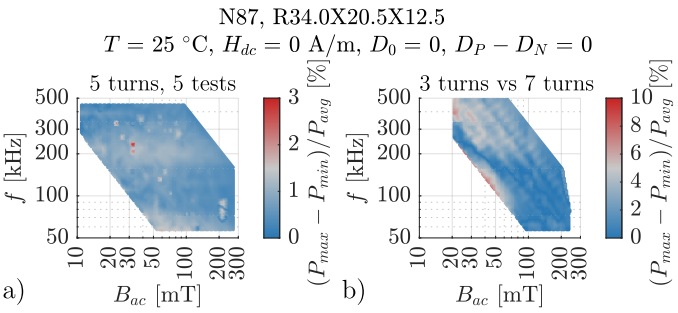

Fig. 37. Reproducibility of the measurements evaluated by the maximum relative variation in losses given by $(P_{max} - P_{min})/P_{avg}$ of the interpolated results for the same core. a) 5 sets of tests. b) For a different number of turns in the regions where data is available for both.

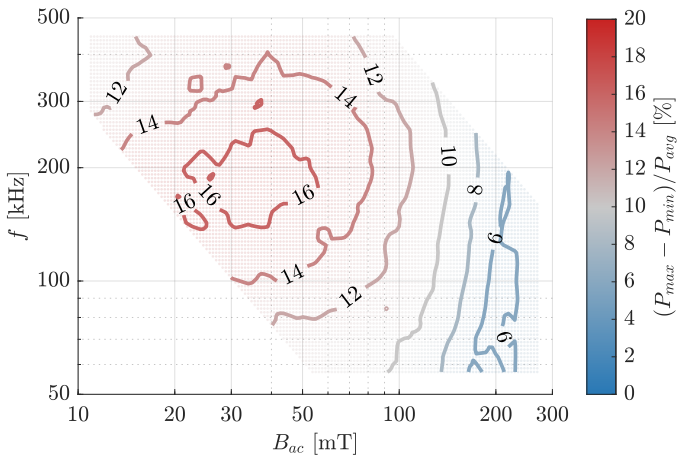

Fig. 38. Contour of the maximum relative variation in losses of the interpolated results for the different R34.0×20.5×12.5 N87 cores tested with triangular 50% duty cycle excitation at 25 °C without dc bias.

waveforms has been repeated 5 times using the same DUT. Core losses can be evaluated to determine the impact that statistical errors have on the system. Fig. 37a shows the variation between the maximum and minimum core losses measured out of the 5 tests. On average, the error is 0.75% spread randomly across the f–B_{ac} plane. The same analysis, but in terms of amplitude permeability gives a maximum variation between the 5 tests below 0.72% on average. As a result, it is concluded that statistical errors in the setup can be safely ignored. Note that the same testing sequence is used for the 5 cases, as such, errors because of magnetic history cannot be assessed.

Similarly, to evaluate how parasitics or the selection of the vertical scale in the oscilloscope affect the quality of the data, the same core has been tested using a different number of turns as suggested in [20]. Instead of 5 turns, 7 and 3 turns have been wound, and the relative variation in core loss between the two tests is shown in Fig. 37b. Up to an 8% difference is measured, although the average is only 2.1%. This value, although not negligible, is acceptable as it is lower than the variation from core to core discussed in the following section.

G. Effect of the variation of the core parameters

B and H are estimated based on A_e and l_e using Eqs. (2) and (3), and volumetric losses are reported based on V_e using Eq. (4). In this work, the effective parameters listed in the datasheet are used. The tolerances of the effective parameters are calculated based on the tolerances on the diameter and height provided for uncoated toroids since the authors could not find any better source for this tolerance. For instance, for the R34.0×20.5×12.5 toroid, the inner diameter d_i is specified as 20.5±0.5 mm, the outer diameter d_o is 34.0±0.7 mm and the height h is 12.5±0.3 mm. The effective parameters, from the IEC-60205 standard [29], are given by:

$$l_e = \frac{\pi \ln \frac{d_o}{d_i}}{\frac{1}{d_i} - \frac{1}{d_o}};\quad A_e = \frac{h}{2}\frac{\ln^2 \frac{d_o}{d_i}}{\frac{1}{d_i} - \frac{1}{d_o}};\quad V_e = \frac{h}{2}\frac{\pi \ln^3 \frac{d_o}{d_i}}{\left(\frac{1}{d_i} - \frac{1}{d_o}\right)^2} \quad (8)$$

The minimum, nominal, and maximum effective lengths are 80.2 mm, 82.06 mm, and 83.92 mm respectively, which represent a ±2.3% tolerance. This error is reflected in the reported H. For the effective area, the values are 73.72 mm^2, 82.6 mm^2, and 91.74 mm^2 for minimum, nominal, and maximum respectively. The impact can be very significant, leading to +10.75%, -11.06% in A_e, implying a $\sim$ ±11% maximum error in the reported $B(t)$. Finally, the effective volume, nominally 6778 mm^3, can be as low as 6070 mm^3 and as high as 7497 mm^3; +10.4% and -10.6%. This effect implies a maximum error in the reported volumetric loss of about 10% too. This error is probably overestimated but data on the tolerance of effective parameters are not readily available. Please note that to lower this error manufacturers would have to provide narrower definitions for the specified distances of the core, or the dimensions of DUTs should be carefully measured. Finally, not only dimensions, but material properties might change from core to core because of slightly different conditions during the manufacturing process. For instance, a tolerance of ±25% for the initial permeability for N87 material is reported in the datasheet, and a variation of 100% in conductivity between two cores is found in [14].

Both the change in effective parameters and core properties affect the behavior of cores. To check the impact of these effects (independent of the measurement system), 5 equal cores bought from the same distributor have been measured, all of them using the same winding configuration listed in Section II-A. The results are depicted in terms of maximum relative variation between tests in Fig. 38, showing a maximum variation of 16% from one core to another, but this variation is not constant in the f–B_{ac} plane. Interestingly, none of the five cores has consistently the highest or lowest core loss, but a core can have higher losses than the other only in certain parts of the f–B_{ac} plane. The same analysis could be performed with the relative amplitude permeability. On average, the maximum discrepancy between the five tests is 7.4%, 10.6% peak, which is within the tolerance specified by the manufacturer for initial permeability. The variation is spread more evenly than the losses so a plot is not needed. This variation in parameters gives an idea of the accuracy that models and measurements should target, and are only worth improving if lower material tolerances are achievable.

ACKNOWLEDGEMENTS

This work was supported by ARPA-E under the DIFFERENTIATE program. We also gratefully acknowledge financial support from the Schmidt DataX Fund at Princeton University made possible through a major gift from the Schmidt Futures Foundation. This project has also received support from Dartmouth College and Plexim GmbH. The authors would like to thank David Radcliff for the design of the fixture for the setup.

REFERENCES

[1] C. O. Mathúna, N. Wang, S. Kulkarni, and S. Roy, "Review of integrated magnetics for power supply on chip (PwrSoC)," *IEEE Transactions on Power Electronics*, vol. 27, no. 11, pp. 4799–4816, 2012.

[2] C. R. Sullivan, B. A. Reese, A. L. F. Stein, and P. A. Kyaw, "On size and magnetics: Why small efficient power inductors are rare," in *2016 International Symposium on 3D Power Electronics Integration and Manufacturing (3D-PEIM)*, 2016, pp. 1–23.

[3] M. Sankarasubramanian, K. Radhakrishnan, Y. Min, W. Lambert, M. J. Hill, A. Dani, R. Mesch, L. Wojewoda, J. Chavarria, and A. Augustine, "Magnetic inductor arrays for Intel® fully integrated voltage regulator (FIVR) on 10th generation Intel® Core™ SoCs," in *2020 IEEE 70th Electronic Components and Technology Conference (ECTC)*, 2020, pp. 399–404.

[4] C. R. Sullivan and M. Chen, "Coupled inductors for fast-response high-density power delivery: Discrete and integrated," in *2021 IEEE Custom Integrated Circuits Conference (CICC)*, 2021, pp. 1–8.

[5] C. Sullivan, "Optimal choice for number of strands in a litz-wire transformer winding," *IEEE Transactions on Power Electronics*, vol. 14, no. 2, pp. 283–291, 1999.

[6] ——, "Computationally efficient winding loss calculation with multiple windings, arbitrary waveforms, and two-dimensional or three-dimensional field geometry," *IEEE Transactions on Power Electronics*, vol. 16, no. 1, pp. 142–150, 2001.

[7] M. Chen, M. Araghchini, K. K. Afridi, J. H. Lang, C. R. Sullivan, and D. J. Perreault, "A systematic approach to modeling impedances and current distribution in planar magnetics," *IEEE Transactions on Power Electronics*, vol. 31, no. 1, pp. 560–580, 2016.

[8] G. Skutt and F. Lee, "Characterization of dimensional effects in ferrite-core magnetic devices," in *PESC Record. 27th Annual IEEE Power Electronics Specialists Conference*, vol. 2, 1996, pp. 1435–1440 vol.2.

[9] M. Kacki, M. S. Ryłko, J. G. Hayes, and C. R. Sullivan, "Measurement methods for high-frequency characterizations of permeability, permittivity, and core loss of mn-zn ferrite cores," *IEEE Transactions on Power Electronics*, vol. 37, no. 12, pp. 15 152–15 162, 2022.

[10] "Ferrites and accessories - N87 material," online; accessed October 2022. [Online]. Available: https://www.tdk-electronics.tdk.com

[11] "TDK Electronics: Ferrite Magnetic Design Tool ver.5.6.1," online; accessed October 2022. [Online]. Available: https://www.tdk-electronics.tdk.com/en/180490/design-support/design-tools/ferrite-magnetic-design-tool

[12] J. Goodenough, "Summary of losses in magnetic materials," *IEEE Transactions on Magnetics*, vol. 38, no. 5, pp. 3398–3408, 2002.

[13] M. Kacki, M. S. Ryłko, J. G. Hayes, and C. R. Sullivan, "Analysis and experimental investigation of high-frequency magnetic flux distribution in mn-zn ferrite cores," *IEEE Transactions on Power Electronics*, vol. 38, no. 1, pp. 703–716, 2023.

[14] T. P. Todorova, A. Van den Bossche, and V. C. Valchev, "A procedure for the extraction of intrinsic ac conductivity and dielectric constant of n87 mn–zn ferrite samples based on impedance measurements and equivalent electrical circuit modeling," *IEEE Transactions on Power Electronics*, vol. 33, no. 12, pp. 10 723–10 735, 2018.

[15] H. Zhao, C. Ragusa, C. Appino, O. de la Barrière, Y. Wang, and F. Fiorillo, "Energy losses in soft magnetic materials under symmetric and asymmetric induction waveforms," *IEEE Transactions on Power Electronics*, vol. 34, no. 3, pp. 2655–2665, 2019.

[16] H. Li, D. Serrano, T. Guillod, S. Wang, E. Dogariu, A. Nadler, M. Luo, V. Bansal, N. Jha, Y. Chen, C. R. Sullivan, and M. Chen, "How magnet: Machine learning framework for modeling power magnetic material characteristics," 2022, iEEE Transactions on Power Electronics [Manuscript under review].

[17] "Princeton-Dartmouth-Plexim MagNet Project: Data-Driven Methods for Power Magnetics Modeling." [Online]. Available: https://mag-net.princeton.edu/

[18] H. Li, D. Serrano, T. Guillod, E. Dogariu, A. Nadler, S. Wang, M. Luo, V. Bansal, Y. Chen, C. R. Sullivan, and M. Chen, "MagNet: An open-source database for data-driven magnetic core loss modeling," in *2022 IEEE Applied Power Electronics Conference and Exposition (APEC)*, 2022, pp. 588–595.

[19] E. Stenglein, B. Kohlhepp, D. Kübrich, M. Albach, and T. Dürbaum, "GaN-half-bridge for core loss measurements under rectangular ac voltage and dc bias of the magnetic flux density," *IEEE Transactions on Instrumentation and Measurement*, vol. 69, no. 9, pp. 6312–6321, 2020.

[20] V. Thottuvelil, T. Wilson, and H. Owen, "High-frequency measurement techniques for magnetic cores," *IEEE Transactions on Power Electronics*, vol. 5, no. 1, pp. 41–53, 1990.

[21] H. Y. Lu, J. G. Zhu, and S. Y. R. Hui, "Measurement and modeling of thermal effects on magnetic hysteresis of soft ferrites," *IEEE Transactions on Magnetics*, vol. 43, no. 11, pp. 3952–3960, 2007.

[22] J. Li, T. Abdallah, and C. Sullivan, "Improved calculation of core loss with nonsinusoidal waveforms," in *Conference Record of the 2001 IEEE Industry Applications Conference. 36th IAS Annual Meeting*, vol. 4, 2001, pp. 2203–2210 vol.4.

[23] E. Stenglein, D. Kuebrich, M. Albach, and T. Duerbaum, "Novel fit formula for the calculation of hysteresis losses including dc-premagnetization," in *PCIM Europe 2019; International Exhibition and Conference for Power Electronics, Intelligent Motion, Renewable Energy and Energy Management*, 2019, pp. 1–8.

[24] P. C. Sarker, M. R. Islam, Y. Guo, J. Zhu, and H. Y. Lu, "State-of-the-art technologies for development of high frequency transformers with advanced magnetic materials," *IEEE Transactions on Applied Superconductivity*, vol. 29, no. 2, pp. 1–11, 2019.

[25] Y. Han and Y.-F. Liu, "A practical transformer core loss measurement scheme for high-frequency power converter," *IEEE Transactions on Industrial Electronics*, vol. 55, no. 2, pp. 941–948, 2008.

[26] C. R. Sullivan, J. H. Harris, and E. Herbert, "Core loss predictions for general pwm waveforms from a simplified set of measured data," in *2010 Twenty-Fifth Annual IEEE Applied Power Electronics Conference and Exposition (APEC)*, 2010, pp. 1048–1055.

[27] E. Stenglein, D. Kuebrich, M. Albach, and T. Dürbaum, "Guideline for hysteresis curve measurements with arbitrary excitation: Pitfalls to avoid and practices to follow," in *PCIM Europe 2018; International Exhibition and Conference for Power Electronics, Intelligent Motion, Renewable Energy and Energy Management*, 2018, pp. 1–8.

[28] P. Welch, "The use of fast fourier transform for the estimation of power spectra: A method based on time averaging over short, modified periodograms," *IEEE Transactions on Audio and Electroacoustics*, vol. 15, no. 2, pp. 70–73, 1967.

[29] "IEC Standard 60205: Calculation of the effective parameters of magnetic piece parts," 2006.

[30] J. Mühlethaler, J. Biela, J. W. Kolar, and A. Ecklebe, "Improved core-loss calculation for magnetic components employed in power electronic systems," *IEEE Transactions on Power Electronics*, vol. 27, no. 2, pp. 964–973, 2012.

[31] F. Preisach, "On the magnetic aftereffect," *IEEE Transactions on Magnetics*, vol. 53, no. 3, pp. 1–11, 2017.

[32] D. Jiles and D. Atherton, "Theory of ferromagnetic hysteresis," *Journal of Magnetism and Magnetic Materials*, vol. 61, pp. 48–60, 1986.

[33] F. Liorzou, B. Phelps, and D. Atherton, "Macroscopic models of magnetization," *IEEE Transactions on Magnetics*, vol. 36, no. 2, pp. 418–428, 2000.

[34] W. Roshen, "Ferrite core loss for power magnetic components design," *IEEE Transactions on Magnetics*, vol. 27, no. 6, pp. 4407–4415, 1991.

[35] A. Laudani, G. M. Lozito, and F. R. Fulginei, "Dynamic hysteresis modelling of magnetic materials by using a neural network approach," in *2014 AEIT Annual Conference - From Research to Industry: The Need for a More Effective Technology Transfer (AEIT)*, 2014, pp. 1–6.

[36] M. Tian, H. Li, and H. Zhang, "Neural network model for magnetization characteristics of ferromagnetic materials," *IEEE Access*, vol. 9, pp. 71 236–71 243, 2021.

[37] E. C. Snelling, *Soft Ferrites, Properties and Applications*. Iliffe, 1969.

[38] W. G. Hurley, T. Merkin, and M. Duffy, "The performance factor for magnetic materials revisited: The effect of core losses on the selection of core size in transformers," *IEEE Power Electronics Magazine*, vol. 5, no. 3, pp. 26–34, 2018.

[39] G. Bertotti, "General properties of power losses in soft ferromagnetic materials," *IEEE Transactions on Magnetics*, vol. 24, no. 1, pp. 621–630, 1988.

[40] J. Reinert, A. Brockmeyer, and R. De Doncker, "Calculation of losses in ferro- and ferrimagnetic materials based on the modified steinmetz

equation," *IEEE Transactions on Industry Applications*, vol. 37, no. 4, pp. 1055–1061, 2001.
[41] M. Luo, D. Dujic, and J. Allmeling, "Modeling frequency-dependent core loss of ferrite materials using permeance-capacitance analogy for system-level circuit simulations," *IEEE Transactions on Power Electronics*, vol. 34, no. 4, pp. 3658–3676, 2019.
[42] C. Baumann, Michaeland Drexler, J. Pfeiffer, J. Schueltzke, E. Lorenz, and M. Schmidhuber, "Investigation of core-loss mechanisms in large-scale ferrite cores for high frequency applications," 2022.
[43] E. Stenglein and T. Dürbaum, "Core loss model for arbitrary excitations with dc bias covering a wide frequency range," *IEEE Transactions on Magnetics*, vol. 57, no. 6, pp. 1–10, 2021.
[44] S. Barg, K. Ammous, H. Mejbri, and A. Ammous, "An improved empirical formulation for magnetic core losses estimation under nonsinusoidal induction," *IEEE Transactions on Power Electronics*, vol. 32, no. 3, pp. 2146–2154, 2017.
[45] K. Venkatachalam, C. Sullivan, T. Abdallah, and H. Tacca, "Accurate prediction of ferrite core loss with nonsinusoidal waveforms using only steinmetz parameters," in *2002 IEEE Workshop on Computers in Power Electronics, 2002. Proceedings.*, 2002, pp. 36–41.
[46] D. Rodriguez-Sotelo, M. A. Rodriguez-Licea, I. Araujo-Vargas, J. Prado-Olivarez, A. I. Barranco-Gutiérrez, and F. J. Perez-Pinal, "Power losses models for magnetic cores: A review," *Micromachines (Basel)*, vol. 13, 2022.
[47] J. Y. Alsawalhi and S. D. Sudhoff, "Saturable thermally-representative steinmetz-based loss models," *IEEE Transactions on Magnetics*, vol. 49, no. 11, pp. 5438–5445, 2013.
[48] S. Barg and K. Bertilsson, "Core loss calculation of symmetric trapezoidal magnetic flux density waveform," *IEEE Open Journal of Power Electronics*, vol. 2, pp. 627–635, 2021.
[49] E. Stenglein, "Messtechnische charakterisierung und vorhersage der kernverluste bei weichmagnetischen ferriten," Ph.D. dissertation, Friedrich-Alexander-Universität, 2021.
[50] A. Brockmeyer and J. Paulus-Neues, "Frequency dependence of the ferrite-loss increase caused by premagnetization," in *Proceedings of APEC 97 - Applied Power Electronics Conference*, vol. 1, 1997, pp. 375–380 vol.1.
[51] A. Brockmeyer, "Experimental evaluation of the influence of dc-premagnetization on the properties of power electronic ferrites," in *Proceedings of Applied Power Electronics Conference. APEC '96*, vol. 1, 1996, pp. 454–460 vol.1.
[52] C. A. Baguley, B. Carsten, and U. K. Madawala, "The effect of dc bias conditions on ferrite core losses," *IEEE Transactions on Magnetics*, vol. 44, no. 2, pp. 246–252, 2008.
[53] W. K. Mo, D. Cheng, and Y. Lee, "Simple approximations of the dc flux influence on the core loss power electronic ferrites and their use in design of magnetic components," *IEEE Transactions on Industrial Electronics*, vol. 44, no. 6, pp. 788–799, 1997.
[54] J. Mühlethaler, J. Biela, J. W. Kolar, and A. Ecklebe, "Core losses under dc bias condition based on steinmetz parameters," in *The 2010 International Power Electronics Conference - ECCE ASIA -*, 2010, pp. 2430–2437.
[55] M. Yang, Y. Li, Q. Yang, Z. Lin, S. Yue, H. Wang, and C. Liu, "Magnetic properties measurement and analysis of high frequency core materials considering temperature effect," *IEEE Transactions on Applied Superconductivity*, vol. 30, no. 4, pp. 1–5, 2020.
[56] W. Grimmond, A. Moses, and P. Ling, "Geometrical factors affecting magnetic properties of wound toroidal cores," *IEEE Transactions on Magnetics*, vol. 25, no. 3, pp. 2686–2693, 1989.
[57] M. Luo, D. Dujic, and J. Allmeling, "Modeling frequency independent hysteresis effects of ferrite core materials using permeance–capacitance analogy for system-level circuit simulations," *IEEE Transactions on Power Electronics*, vol. 33, no. 12, pp. 10 055–10 070, 2018.
[58] M. Mu, Q. Li, D. J. Gilham, F. C. Lee, and K. D. T. Ngo, "New core loss measurement method for high-frequency magnetic materials," *IEEE Transactions on Power Electronics*, vol. 29, no. 8, pp. 4374–4381, 2014.
[59] Tektronix, "MSO4000 and DPO4000 Series Digital Phosphor Oscilloscopes - Specifications and Performance Verification," online; accessed October 2022. [Online]. Available: https://download.tek.com/manual/077024701Rev_A_web.pdf
[60] E. Stenglein, D. Kübrich, M. Albach, and T. Dürbaum, "Influence of magnetic history and accommodation on hysteresis loss for arbitrary core excitations," in *2019 21st European Conference on Power Electronics and Applications (EPE '19 ECCE Europe)*, 2019, pp. P.1–P.10.